University of Illinois at Urbana-Champaign

ACRC

Air Conditioning and Refrigeration Center A National Science Foundation/University Cooperative Research Center

Analysis of design tradeoffs for display case evaporators

R. Chandrasekharan and C. W. Bullard

ACRC CR-55 October 2004

For additional information:

Air Conditioning and Refrigeration Center
University of Illinois
Mechanical & Industrial Engineering Dept.
1206 West Green Street
Urbana, IL 61801

(217) 333-3115

The Air Conditioning and Refrigeration Center was founded in 1988 with a grant from the estate of Richard W. Kritzer, the founder of Peerless of America Inc. A State of Illinois Technology Challenge Grant helped build the laboratory facilities. The ACRC receives continuing support from the Richard W. Kritzer Endowment and the National Science Foundation. The following organizations have also become sponsors of the Center.

Alcan Aluminum Corporation
Arçelik A. S.
Behr GmbH and Co.
Carrier Corporation
Cerro Flow Products, Inc.
Copeland Corporation
Daikin Industries, Ltd.
Delphi Thermal and Interior
Embraco S. A.
Ford Motor Company
Fujitsu General Limited
General Motors Corporation
Hill PHOENIX
Hydro Aluminum Adrian, Inc.
Ingersoll-Rand/Climate Control
Lennox International, Inc.
Manitowoc Ice, Inc.
LG Electronics, Inc.
Modine Manufacturing Co.
Parker Hannifin Corporation
Peerless of America, Inc.
Samsung Electronics Co., Ltd.
Sanden Corporation
Sanyo Electric Co., Ltd.
Tecumseh Products Company
Trane
Visteon Automotive Systems
Wieland-Werke, AG
Wolverine Tube, Inc.

For additional information:

Air Conditioning & Refrigeration Center
Mechanical & Industrial Engineering Dept.
University of Illinois
1206 West Green Street
Urbana, IL 61801

217 333 3115

ABSTRACT

A model for simulating a display case evaporator under frosting conditions has been developed, using a quasi-steady and finite-volume approach and a Newton-Raphson based solution algorithm. It is capable of simulating evaporators with multiple modules having different geometries, e.g. fin thicknesses and pitch.

The model was validated against data taken at 2-minute intervals from a well-instrumented medium-temperature vertical display case, for two evaporators having very different configurations. The data from these experiments provided both the input data for the model and also the data to compare the modeling results. Redundant data was available, and was used to further analyze the data.

The validated model has been used to generate some general guidelines for coil design. Effects of various geometrical parameters were quantified, and compressor performance data were used to express the results in terms of total power consumption. Using these general guidelines, a new prototype evaporator was designed, keeping in mind the current packaging restrictions, tube and fin availabilities, and is an optimum coil for the given external load conditions. Further, the validated model was used to arrive at prototype coils with some of the current tube and fin spacing restrictions removed.

Table of Contents

List of Figures

Page

List of Tables

Page

Nomenclature

A	surface area, m^2
cfm	air flow rate , *cfm*
C	Heat capacity, J/K
COP	coefficient of performance
c_p	specific heat of moist air, *kJ/kg.K*
DAG	Discharge air grill
DAT	Temperature measured at the DAG
DX	Direct expansion
dP	pressure drop, *Pa*
EER	Energy efficiency ratio
EES	Engineering Equation Solver, software
EEV	Electronic expansion valve
f	infiltration fraction
fpi	fins per inch
K_a	thermal conductivity of air, *kW/m.K*
k_{fr}	thermal conductivity of frost, *kW/m.K*
Le	Lewis number, α/D
$\dot{m}_{fr}$	frost deposition rate, *kg/s*
$\dot{m}_{air}$	air mass flow rate, *kg/s*
$\dot{m}_{ref}$	refrigerant mass flow rate, *kg/s*
Q	load, *kW*
RAG	Return air grill
RTD	Resistance Temperature Detector
SCE	Southern California Edison
SLHX	Suction Line Heat Exchanger
T	temperature, *°C*
TXV	thermostatic expansion valve
t	time, *sec*
$\dot{V}$	volumetric flow rate, m^3/s
V_{max}	velocity of air based on free flow area, *m/s*
w	air absolute humidity, kg_{water}/kg_{air}
$\dot{W}$	power, *kW*

Greek symbols

ε	effectiveness, dimensionless
ρ	density, kg/m^3
ρ_{fr}	density of frost, kg/m^3
δ_{fr}	frost thickness, *m*
ΔP	pressure drop, kPa
τ	time

Subscripts

a, air	air
amb	evaluated at store ambient air temperature
av	evaluated at average inlet and outlet conditions
combined	Sum of accessory and radiation
comp	compressor
defrost	defrost
dis	evaluated at case discharge air grill
duct	display case duct from coil exit to honeycomb (case discharge)
evap	evaporator
fan	evaporator fan
fr	frost
hx	heat exchanger
in	inlet
max	maximum
metal	coil (fin plus tube)
o	overall (fin and tube)
out	outlet
off	off-cycle
r, ref	refrigerant
ret	evaluated at case return air grill
si	base of the fin (i.e. tube outer surface)
so	frost surface (fin or tube)
tube	tube

Chapter 1. Introduction

This document aims to present the validation and the results of a numerical design tool for a display case evaporator. The most significant aspect of current display case evaporators is the frost accumulation and the resultant change in air-side heat transfer and pressure drop characteristics. The change in air-side pressure drop due to frosting leads to higher fan power requirements and also results in lower airflow rate through the air curtain wherever constant speed fans are used. Any drop in air-curtain airflow leads to higher infiltration and hence higher latent and sensible loads on the evaporator.

Early research on the effect of moisture in the air supplied to coils was done experimentally. Most research done on frosting either studies effect of frost growth or studies the effect of frost growth on coil performance. Research done on frost growth characteristics involves study of properties of frost growing on typical structures like flat plates. (e.g. Mao et al. (1999), Hayashi (1977), Storey and Jacobi (1999), Ostin and Andersson (1991), Yonko and Sepsi (1967)). A comprehensive review of the effect of frosting on heat exchangers is provided by Kondepudi and O'Neal (1987) who also investigated the frost growth effects on the performance of heat exchangers with flat and louvered fins. Tassou and Datta (1999) studied frosting of multi-deck display case evaporator defrost intervals as a function of ambient humidity. Carlson et al. (2001) experimentally studied frosting of a secondary refrigerant based evaporator of geometry similar to those used in display cases. The main aim was to understand the effect of ambient temperature, humidity and other operating conditions on frost deposition and distribution. Ogawa, Tanaka, and Takeshita (1993) studied ways to improve heat exchanger performance under frosting conditions, including staging, cutting, and/or extending the fins.

Most of these results focused on heat exchangers very different from those typically used in supermarket display cases. Most of the early experiments were conducted on single row heat exchangers which lead to lack of data for frost distribution. Also they lacked information regarding the effect of ambient conditions on frost deposition.

There is a lot of modeling work done for condensation in a/c coils but modeling of frosting in heat exchangers is much more limited. Modeling of frost has mostly focused on models of frost deposition on cold surfaces such as flat plates or single cylinders. A few examples of this are Tao et al (1993), Padki et al (1989). A few researchers did look at frost modeling of heat exchangers, but apart from Wu (2001) and Verma (2002), most looked at heat exchangers used for heat pumps or refrigerators and not display cases.

The most significant issue in modeling of display case evaporators is the fact that the geometries of current heat exchangers lie outside the range of available correlations for heat transfer and pressure drop. This necessitates use of finite volume or finite element techniques to model the heat exchangers. The benefit of using such a finite volume technique is that modeling of variable fin spacing and heat exchangers with more than one module in the air flow direction is a trivial task.

The modeling of the display case evaporator is not made more complicated when the evaporator is considered as part of a larger system that includes the air curtain. The evaporator model depends on the other components to provide the inlet conditions to the evaporator and the load. Once the inlet conditions are set, the modeling of the evaporator is essentially uncoupled from the issue of air curtain and load optimization.

In this document, the model's structure and associated issues are addressed first. The validation of the EES based model against data collected by Southern California Edison (Faramarzi et al. 2003) is presented next. Then the design tool is used to arrive at general recommendations for evaporator design when the inlet conditions are known. Finally the design tool and the recommendations are used to arrive at improved designs for evaporators.

Chapter 2. The Numerical Model

The numerical model uses a quasi-steady finite-volume approach. That is, the input from one time step is used as the input to the next time step. The following subsections deal with the capabilities of the model, the required assumptions, the structure of the model and related details.

2.1 The Capabilities of the model

The model is built to simulate DX evaporators. The model provides the frost distribution and the other air-side and refrigerant-side parameters as a function of time. The model deals with the fin and tube heat and mass transfer separately and hence provides values for both fin and tube frost thicknesses. Given that the finite volume technique used follows the air-side geometry, the model can trivially handle variable fin spacings and variable fin thicknesses. It can also handle more than one module in the airflow direction. This allows us to explore the effect of boundary layer restarting on the performance of the evaporator.

The model can handle both constant airflow fans and constant speed fans. When constant speed fans are used, it is necessary to provide the model with the fan performance curves. It is also necessary to provide the value of infiltration load as a function of the airflow rate. When constant airflow rate fans are used, this is not necessary as the infiltration load remains constant.

2.2 Assumptions made in the model

Apart from the fact that a finite volume approach is used, a few assumptions are necessary to simplify the modeling.

1. Frost growth modeling is simplified by considering only mature frost growth. This is done by assuming a certain initial frost layer (0.00005 mm thick) on the fins and tubes. This assumption eliminates the need to model the complex early crystal growth period. The frost surface roughness effect which increases the surface area is also neglected because it is significant only in early frost modeling.
2. Within any given finite volume, the value for fin frost thickness or tube frost thickness is the same everywhere.
3. When the frost surface temperature reaches 0 °C, the density of the frost can be linearly extrapolated until it rises to the density of ice at 0 °C (920 kg/m^3) while the thickness of the frost remains constant. Once the density of frost reaches the density of ice, the thickness of the frost increases while the density of the frost remains constant.
4. Frost density is assumed to only increase and never decrease. In other words, it is assumed that the frosting is monotonic. The freeze thaw cycles observed by some researchers [Raju, 1993] are not modeled. The reason for this assumption is elaborated in subsection 2.4
5. Only the leading edge finite volume contains a superheated segment. This is justified because of the small values of superheat normally employed in display case evaporators. Also the refrigerant properties for the leading edge finite volume are calculated assuming the refrigerant to be single phase. This is justified because the walls are generally dry in the high quality regions of the evaporator.

2.3 Heat and mass transfer modeling, correlations used

The governing equations for the heat and mass transfer modeling are the energy balance equations and the continuity equation applied to the fins and the tubes of each of the finite volumes. For example, the mass transfer rate was calculated by solving simultaneously the continuity and the one-dimensional mass transfer equations for fins and tubes separately for each of the finite volumes.

$$\dot{m}_{fr} = \dot{m}_{air}(w_{in} - w_{out}) \tag{2.3.1}$$

$$\dot{m}_{fr} = (h_a \cdot Le^{-2/3} / c_{p,a}) \cdot A_o \cdot (w_{av} - w_{so}) \tag{2.3.2}$$

Figure 2.3.1 shows a fin and tube surface covered with frost. The heat transfer modeling is done by considering a two lump model to simulate the heat transfer through the frost layer. For each segment, the one-dimensional sensible heat transfer is computed using the average temperature of air flowing through the segment. This was solved simultaneously with the air-side energy balance. Latent heat transfer resulted from the formation of frost on the surface of tubes and fins. The total heat transfer was determined by solving simultaneously the equations for conduction through the frost layer, heat transfer from the tube to refrigerant and refrigerant-side energy balance.

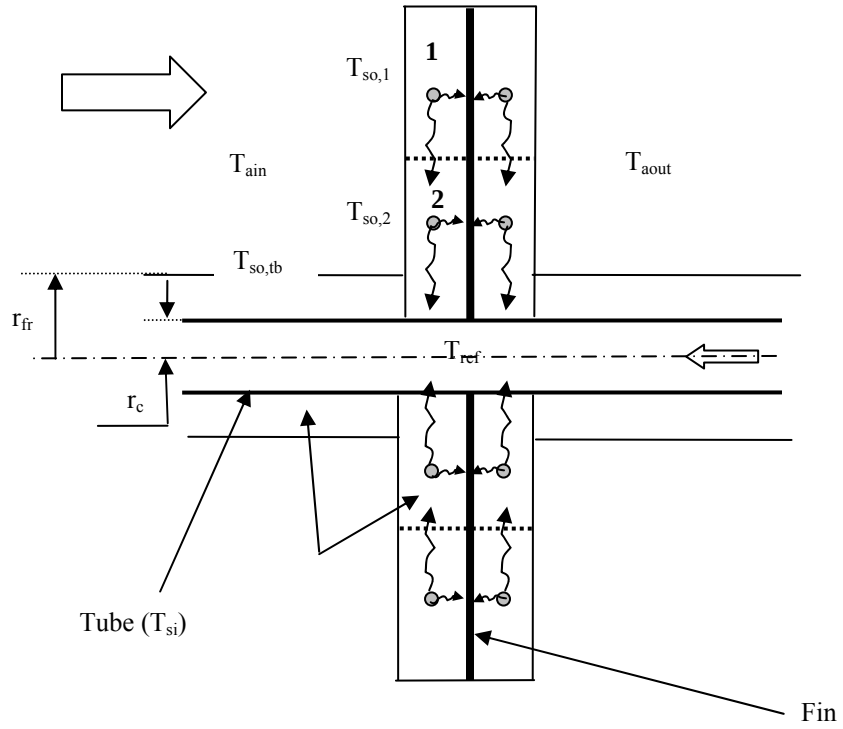

Figure 2.3.1 Heat transfer through the frost, tube and fin

The frost surface temperatures, the frosting rate and the air and refrigerant outlet states are obtained by simultaneously solving the heat and mass transfer equations. The fin and tube incremental frost mass was used to calculate the fin and tube incremental frost thickness. This incremental frost was then added to the frost layer already existing on the fin and tube surfaces. Finally the density and conductivity of frost on fins and tubes to be used for the next time step was computed using the existing frost thickness.

Thus the essence of the model is to determine the frost surface temperature by solving simultaneously the separate equations for the convective heat (sensible) and mass (latent) transfer between ambient air and the frost surface. The total heat transfer is analyzed for conduction within the frost layer using the two-lump method. Using three lumps instead of two did not change the answer by more than 1% and hence the 2 lump method was used.

The solving of the above described equations assumes knowledge and availability of correlations to calculate the air-side heat transfer & pressure drop coefficients, frost density, frost conductivity and refrigerant heat and pressure drop coefficients. They are described in the below subsection. Issues regarding their use and limitations are also addressed as they crop up.

2.3.1 Correlations used

1. Frost density

Hayashi's (1976) empirical correlation is used to determine frost density when the frost surface temperature is below freezing.

$$\rho_{fr} = 650\, e^{0.277\, T_{so}} \qquad (2.3.1.1)$$

This empirical correlation has 2 known limitations. One is that it fails below -10°C. This one is not encountered in modeling of any of the display case evaporators for reasonable run times. It can be handled by assuming a constant frost density below -10 °C. Another limitation of this correlation arises when the frost surface temperature rises to freezing temperature (0°C), for a particular finite volume. In such a case there is an occurrence of repeated cycles of melting and refreezing once the frost surface temperature reaches the freezing point, (Raju (1993)). The complexity of the structural changes of the frost along with the lack of literature forces a simplifying assumption. For any finite volume where the frost surface temperature reaches the freezing point, the model assumes that the frost density would ultimately reach the density of ice at the freezing point, with the water continuously seeping into the porous frost layer increasing its density and the frost thickness remains constant (i.e. no incremental frost thickness). Once the frost density reaches the density of ice (920 kg/m^3), it is held constant while the frost thickness increases. Thus the Hayashi correlation which is better suited to applications from -9 °C to -1°C is being extended to the whole range of temperatures encountered. Moreover, there are no other correlations available in this temperature range. Hence the frost density values are suspect to a certain degree.

2. Frost conductivity

The thermal conductivity of frost was determined by employing the Yonko and Sepsy (1967) correlation between the frost conductivity and frost density which is

$$k_{fr} = (0.02422 + 7.214 \cdot 10^{-4} \cdot \rho_{fr} + 1.1797 \cdot 10^{-6} \cdot \rho_{fr}{}^2)/1000 \qquad (2.3.1.2)$$

The correlation is limited to ρ_{fr} < 576 kg/m^3. However their correlation when extrapolated to the density of ice predicts the thermal conductivity of ice within 10 % of the tabulated values and hence is used for entire range of frost densities encountered. This assumption could add to an equally significant difference in the heat transfer values.

3. Air-side heat transfer coefficient

The coils in display cases are roughly 10 to 12 rows deep crossflow heat exchangers. Most correlations available in literature have been developed from experiments on coils which are much shorter in the airflow direction. There are no available correlations applicable to the entire range of geometries and operating conditions typical of display case evaporators. Verma et al (2002) describe the methodology of selecting air-side heat transfer coefficients. The analysis done for this project was similar though the final choice of correlations was slightly different.

It is possible to assume that the average air-side heat transfer coefficient is unaffected by the extra rows on the air-side. The standard correlations for determining the air-side heat transfer coefficient have been given by Wang and Chang (2000) and Granryd (1999). The Wang and Chang correlation is suitable for fin pitches up to 8-9 mm and hence suitable for use in coils (or modules) with 3 or 4 fpi. But when the coil has 2fpi fin spacing, the same correlation is not valid. In such cases the Granryd correlation (1999) is valid but there are certain shortcomings. The correlation is based on experiments on coils only 3 to 4 rows deep and hence the certainty on the values is low.. However, this correlation tries to incorporate the actual physics involved in the flow and is not simply a curve fit of available evaporator designs. Hence, to check the validity of extrapolating the Granryd correlation to a depth of up to 12 rows, the value based on Granryd and the value calculated using a simple superposition of tube and fin heat transfer coefficients are compared. The comparison between the two is within 15% for coils of 2, 3 and 4 fpi up to 12 rows deep. Also, the values compare very well with the predictions of Wang and Chang in that part of the range where it is valid. Thus, the use of Granryd's correlation is justified for coils of upto 12 rows depth and for any of the commonly used fin densities (i.e. 2 to 5 or 6 fpi).

The use of average heat transfer coefficients leads to underprediction of the local heat transfer coefficients at the leading edges and the leading edge control volumes of the coil. This leads to a gross underprediction of the frost thickness at the point where the boundary layer restarting occurs. Alternately, it is possible to calculate something similar to a local heat transfer coefficient for each of the finite volumes. For any finite volume, the "local" heat transfer coefficient can be assumed to be the contribution of that finite volume to the average heat transfer coefficient. This can be calculated by using the following relation for the n^{th} finite volume in terms of the average heat transfer coefficients

$$h_{finite,volume,n} = \left(n * h_{average,n}\right) - \left((n-1) * h_{average,n-1}\right) \qquad (2.3.1.3)$$

Use of such a formulation for calculation of heat transfer coefficient enables us to capture the locally high heat transfer coefficient at the leading edges of the modules of the coil. Care must be taken to use the correct number of rows to calculate each of the above average heat transfer coefficients. When the coil is split into two or more modules, the downwind modules are in the wake of the first module and hence restarting of the boundary layer occurs only when there is sufficient space between the two modules so that there is room for the velocity profile to approach uniformity.

Thus, the heat transfer coefficient for any finite volume is calculated as the contribution of that finite volume to the average heat transfer coefficient. For calculating the average heat transfer coefficients, Granryd's correlation and these local properties are used.

4. Air side pressure drop

For air-side pressure drop the correlations of Wang et al. (2000); and Granryd et al. (1999) were considered. The Granryd correlation was used to compute the air-side pressure drop. The reasons for the choice are detailed in Verma (2002).

5. Refrigerant side heat transfer coefficient

For the finite volumes with refrigerant in single phase flow, Gnielinski's (1976) correlation for fully developed turbulent flow in a circular tube was used while for two phase flow with quality less than 85 % Wattelet and Chato (1994) correlation was utilized. For near saturated refrigerant (with more than 85 % quality), a linear interpolation between Wattelet and Chato (1994) and Gnielinski (1976) was utilized to determine the refrigerant side heat transfer coefficient.

6. Refrigerant side pressure drop

For tubes with two phase refrigerant flow the Souza and Pimenta (1995) correlation was used to determine the refrigerant frictional and acceleration pressure drops. For single phase flows in the transition or turbulent regime, the refrigerant side pressure drop was determined using Darcy's friction factor based on Churchill's (1977) correlation, while in the laminar region the friction factor was calculated using the relation $f=64/Re$.

2.4 Modeling related issues

There is a complicated interdependence among the parameters of a heat exchanger. This leads to the governing equations becoming nonlinear and simultaneous. The nonlinearity is introduced by heat mass transfer equations while the simultaneity is the result of the interdependence. The interdependence coupled with the fact that a quasi-steady approach is used leads to a potentially unstable model with robustness issues. The following 2 subsections deal with these issues

2.4.1 Robustness of the model: dealing with noisy experimental data

The quasi-steady model is solved using a simultaneous solver (Engineering Equation Solver, EES). This solver makes use of an iterative Newton Raphson procedure. The Newton-Raphson method is among the best available methods to solve a large number of nonlinear simultaneous equations. However the method is highly sensitive to the guess values for the various unknowns especially if the number of equations is large and the interdependence among the various unknowns is complicated and highly nonlinear. The frosting model has parameters at any time step that must be calculated from the solution for the previous time step.

Thus, the user supplies initial guess values for the variables. Using these guess values and initiation values for frost thickness and density, the first time step is solved and the Newton-Raphson algorithm updates the guesses. This procedure continues with the solution from t_n providing guesses for t_{n+1}. The updating process is done by Newton-Raphson and these updated guesses can at times fail to provide sufficiently good guess values for the next time step. Thus if the change in the input variables from one time step to the next is large, this can cause a problem. Such a situation usually arises when the inputs are obtained from noisy experimental data. A specific example encountered while simulating the Hill Phoenix coil is explained below. The way the problem was solved throws light on a general strategy that can be used to overcome such problems

During the running of the model, it was observed that even small changes in the refrigerant inlet temperature caused the model to crash. The problem was traced back to the two phase heat transfer calculations.

The guess values for the refrigerant pressures for certain time steps were causing the quality to assume values greater than 1 during the iterations within that time step causing the model to fail. A simple fix for this problem was to include an if-then loop in the 2-phase heat transfer procedure which set the quality to some value close to .99 whenever the quality passed to the procedure was greater than one. This allows the model to proceed with its iterations without being stopped due to a bad guess. The setting of the value of the quality to a particular value does not imply an arbitrary assignment of value to the quality. The final answer will be such that the physical requirement on the system of equations is satisfied. The assignment of a particular value to the quality serves purely as an intermediate step that enables the code to iterate without being stopped. Thus by fixing secondary symptoms, the original problem can be handled within the Newton-Raphson framework.

2.4.2 Problem of oscillations introduced as time progresses

The values calculated for many of the physical variables start fluctuating about the mean as the frosting period progresses. The oscillations start off because of reasons not well understood (could be anything from actual physics to a simple accumulation of round-off errors). But the reason for the continuation and worsening of the oscillations is much better understood. The dependence of parameters like the density of the frost and hence the outer dimensions of the heat exchanger tubes and fins on the frost temperature, combined with the fact that every time run depends on the prior time run for its calculations, was found to the reason behind the spiraling nature of the oscillations and the reason for their continuance. If the solution for any iteration registers a drop in the frost surface temperature which implies a lower frost density and lower frost thickness, the next iteration will have a geometry which is of smaller dimensions than the prior one. This will cause many parameters like the airflow velocity, air-side heat transfer coefficient to increase, causing the frost surface temperature to increase. Thus a local variation begins at this particular point in space and time.

Lack of certainty as to whether the frost surface temperature ever decreases in practice precluded a fix where the frost surface temperature is never allowed to fall. The algorithm was therefore modified by specifying that density alone is not allowed to decrease. Given the way frost builds up this is a reasonable assumption to make. It is not expected that the frost density decreases and then increases again within a span of a few minutes. This does not prevent the frost surface temperature from varying in the positive and negative directions during Newton-Raphson iterations. All it does is to ensure that the interdependence of the variables does not cause the model to go unstable.

This fix caused the variations to disappear. The frost surface temperatures do not drop except in a few runs (2 or 3 in more than 200). This confirms the hypothesis that the observed instabilities were numerical rather than physical

The above portion of this chapter described the heat and mass transfer modeling and associated issues. The next subsection describes in short how the evaporator itself is modeled when it is viewed as part of the larger display case system.

2.5 Simulating the evaporator as part of the entire display case

Open multi-deck display cases are refrigerated spaces separated from the store ambient by means of an air curtain. The process of designing a display case involves designing not only the evaporator coil but also the other

components like the ducts and fans, which must meet the air flow requirements of both the air curtain and the coil. The interaction among the components has to be considered while designing them.

Figure 2.5.1 gives a brief outline of the steps involved in simulating/designing the display case. The basic idea is that the coil simulation/design process and the air flow rate selection can be viewed essentially separable, if a few minor approximations are made.

The airflow rates are arrived at by considering the air flow through the evaporator to be divided into two independent streams. The first of these streams is the flow via the back panel over the products. This stream is the medium of heat transfer interaction for the loads and the air flowing through the refrigerated space. It removes the radiation load incident on the products and also removes the loads due to conduction, lighting and heating. Thus the back panel flow rate can be arrived at by knowing the non infiltration loads on the display case. The other stream is the flow through the discharge air grill. The main consideration while designing this stream is the reduction of infiltration. The value for the air flow through the DAG is arrived at by minimizing the infiltration. Thus the airflow rates are decided once the loads and the air-curtain stability criteria are known. Once the airflow rates and the loads are fixed, the air inlet conditions to the evaporator are fixed. If the refrigerant inlet conditions are known, the evaporator can be simulated.

Thus, the simulation/design of the coil is dependent on the loads and airflow rates. Once the inlet conditions are known over time, evaporator simulation can be carried out independent of the other components. Thus the other components of the display case system can be viewed as the factor deciding the inlet conditions to the coil and once these inlet conditions are known, they do not directly enter the simulation the evaporator. This simplifies the actual evaporator simulation.

The output of the simulation includes values for the required fan and compressor power, the mass of frost, the frost distribution and the thermal mass of the evaporator. These variables are available as a function of time and can be used as the input to an optimization algorithm that arrives at an optimum defrost time. The same algorithm can be extended to arrive at a geometry for a given defrost strategy.

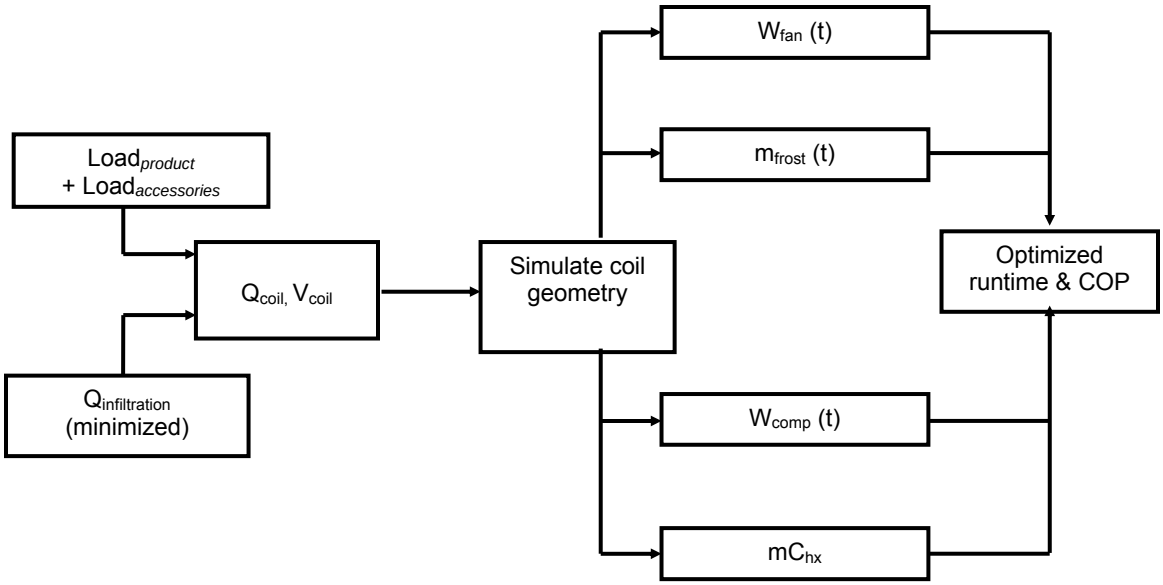

Figure 2.5.1 Outline of simulation/design steps

Chapter 3. Validation

Data for validation was provided by Southern California Edison (Faramarzi et al, 2003). The data sets were the results of experiments on 2 coils, the original Hill Phoenix coil, (November 2002) and the first prototype coil, Prototype-1, provided by Wolverine and Super Radiator Coils (March. June, August, September 2003). The experiments were conducted in an OHM ^{TM} medium temperature multi-deck display case provided by Hill-Phoenix.

This section provides a basic outline of the validation process without presenting the details. The details of each of the steps detailed here are provided in Appendix A.

3.1 Selection of inputs

The first step of the validation process consisted of analyzing all the available data streams and choosing the most relevant and reliable among them as inputs to the simulation model.

The data sets from SCE consisted of around 125 data streams. The measurements were taken at 2 minute intervals for a complete cycle between two defrosts (which is 7 hours for the Hill Phoenix test and 3.5 hours for the Prototype-1 tests). The available measurements included the air and refrigerant temperatures at the inlet and exit of the coil, air velocity measurements, tube surface temperatures, product temperatures, air-side pressure drop readings, condensate mass readings and accessory power consumption. The biggest issues faced while analyzing and choosing input data was the non-uniformity of data from left end to right end of the 8 ft coil. Most notably, the air temperatures varied by as much as 3.5-4 C from left to right. The possibility of faulty equipment was ruled out by looking at the consistency of this observation in independent data sets. Hence the data values were averaged and a single value was arrived at. Also, the mass flow rate and a few other readings had short-period time variations in the latter part of the cycle. By a null hypothesis methodology, these variations were attributed to the controls being used and a curve fit was used to describe these portions of the data sets. A further complication was the absence of reliable air-side pressure drop readings in all of these data sets. This necessitated the use of energy balances in order to find dry coil air flow rates which were then subsequently used in conjunction with the fan curves provided by Hill Phoenix and SCE. Keeping in mind the relative reliability of the individual data streams, the following were chosen as the inputs to the simulation

Geometry of the coil
Air inlet temperature
Initial air flow rate along with the fan curve and duct pressure loss
Refrigerant inlet enthalpy and exit pressure
Relation between infiltration and airflow rate.

3.2 Additional information from the experimental data

Apart from the air and refrigerant properties, the other inputs like the initial airflow rate, infiltration, etc are not directly available. Most of these are arrived at using energy balances. The energy balances and their results are presented in detail in Appendix B. The initial dry coil air flow rate was estimated to be 790 cfm for the original coil. The same energy balances provided values for the loads due to radiation, accessories and other such sources, which were not directly measured by the experiments. Also, the duct pressure loss coefficient was predicted to be 90 by

analysis of the available data. This value was used while designing newer coils. It must be noted that this method of using energy balances is used only due to the non availability of reliable data.

3.3 Comparison of experimental data and modeling results

The comparison of the model and experimental values was preformed for all the available data sets. Both the original Hill Phoenix coil and the Prototype-1 coil lead to the same conclusions. Without presenting the actual comparisons, the most notable conclusions are presented here. The following is the gist of the model's capabilities and failings

1. To achieve a particular discharge air temperature, the model predicts a lower evaporating and surface temperature than suggested by the experimental values.
2. The amount of frost predicted matches within 4%
3. The model airflow rate does not decay as fast as suggested by the energy balance. This could be due to frost densities being overestimated or due to faulty fan curves or even due to the pressure drop correlations being used. The most probable answer is a combination of these factors with the fan curve issue being the biggest contributor. The frost density correlation is uncertain given that the Hayashi correlation is based on experiments performed for lower temperatures than being used here. The evaporator pressure drop correlations have been verified using data from Super Radiator coil.
4. The model predicts the trends of the various parameters very well
5. The difference in simulated and experimental air temperatures is around 1-2 C

It may appear that the large difference in the air-side temperature predictions is a serious shortcoming. But it has to be viewed in the right perspective. The measured air temperature at the inlet to the coil differs by as much as 3-4 C between the left and right sides of the coil inlet and the velocities apparently differ by almost a factor of 2. This coupled with the fact that air-side heat transfer coefficients and pressure drop coefficients have a 20% error margin makes the 1-2 C difference in predictions appear reasonable.

A simple calculation of the various resistances between the refrigerant and the air flowing over the evaporator is sufficient to find the root source of the errors in validation. The resistance between the air and refrigerant (shown by the schematic in Figure 2.3.1) is the sum of the resistance across the frost, metal of the evaporator and the resistance from the frost surface to the free air flowing above (i.e. that represented by the air-side heat transfer coefficient).

At the standard test condition shown, the calculated resistance from the air to outer surface of the frost is 1.5 C while the resistance across the frost and metal is around 0.75 C for Prototype-1. Since the calculated refrigerant-side resistance is small and fairly certain, the air-side heat transfer coefficient would have to be underestimated by 40% or more to explain the difference between the measured and predicted. Therefore it is likely that the uniform air-flow assumption is the major factor contributing to the difference between measured and predicted evaporator performance.

Chapter 4. General Guidelines for Comparing Coils

This section first outlines the performance metrics for comparison of various coil designs. The second part of this section deals with the parameters chosen for designing an improved coil.

4.1 Performance based comparisons

Since lower energy consumption is the goal, the most obvious variables to focus on are the compressor and fan power consumption. But given that fan and compressor energy consumption are functions of runtime, which itself is a function of the frosting rate, the total energy consumption is the appropriate objective function. The following discussion, however, shows that it is indeed sufficient to focus on compressor and fan power values for the range of coils considered.

The total energy consumption is the sum of the energy required to meet the steady on-cycle load plus the energy spent during the off-cycle for defrosting and for dealing with off-cycle loads. The procedure used to arrive at a numerical value for each of these loads along with their effect on total energy consumption is presented here.

The power consumed during the on-cycle is the sum of compressor and fan power required to meet the steady load on the system. This is directly obtained from the system simulation model. No extra mathematical relations are necessary to compute the on-cycle energy for a single cycle. However the per day on-cycle energy consumption does depend on the number of cycles in a day, which is a function of the off-cycle time required to defrost the coil. The equation to calculate the off-cycle period is derived in the further paragraphs.

Melting of accumulated frost is due to forced convection from the surface of the frost. During the off cycle, the flow path of the air is the same as during the on-cycle. Hence the store air still mixes with the air-curtain flow resulting in a return air temperature higher than the discharge air temperature. The difference now is that the discharge air temperature is warmer compared to the on-cycle time when the refrigerant was flowing. Part of this off-cycle infiltration load results in the warming of the metal of the heat exchanger, products, ducting etc. This heating of the products and the metal places an additional load on the system during the subsequent on-cycle. The additional load on the system is a function of the off-cycle period (τ_{off}) which in turn is a direct function of the thermal mass of the frost and the evaporator. These two are dependent on the run-time between defrosts (τ_{on}) and the design of the heat exchanger respectively.

The off cycle time is calculated as the time required to raise the temperature of the evaporator and frost to 0 C and melt the frost. For simplicity, the calculation is done using a thermodynamic end state analysis. The resulting formula for τ_{off} is given by

$$\tau_{off} = \frac{\left(m_{fr} \cdot \Delta h_{if}\right) + \left(C_{frost} \cdot \Delta T_{frost,0}\right) + \left(C_{HX} \cdot \Delta T_{HX,0}\right)}{\varepsilon \cdot \dot{m}_{air} \cdot C_{p,air} \cdot \Delta T_{\max}} \qquad (4.1.1)$$

where $\Delta T_{fr,0}, \Delta T_{HX,0}$ give how much the frost and metal temperatures are below 0 C, i.e. the difference between the temperatures of the frost and the heat exchanger metal at the end of the on-cycle and 0 C. ε is the effectiveness of heat transfer between the frost surface and the air flowing over the frost. $\Delta T_{\max}$ is the maximum temperature difference between the frost surface temperature and the air flowing over the coil. For this purpose, the air

temperature is assumed to be the average of the temperature at the end of the on-cycle and that corresponding to air flowing over a 0 C surface. Similarly the values for the effectiveness are calculated as the average over the time period of the off cycle.

The value obtained for τ_{off} is used to estimate the penalty due to reheating of the evaporator metal and the products. This heating of the metal of the evaporator is a necessity in order to melt the frost, but the heating of the products is an add-on and is purely detrimental. In fact, the temperature of the product reached during the off cycle is a primary constraint on the run time of the coil and hence on coil design and operating considerations. This heating of the metal and products has to be dealt with in the subsequent on-cycle. Given that the DAT could be warmer by as much as 8 C than normal operating temperatures, there is an additional infiltration load (for simplicity, we assume the air infiltration fraction itself to be unaffected by the changes in temperature). The estimation of this additional load on the system is done using the following energy balances.

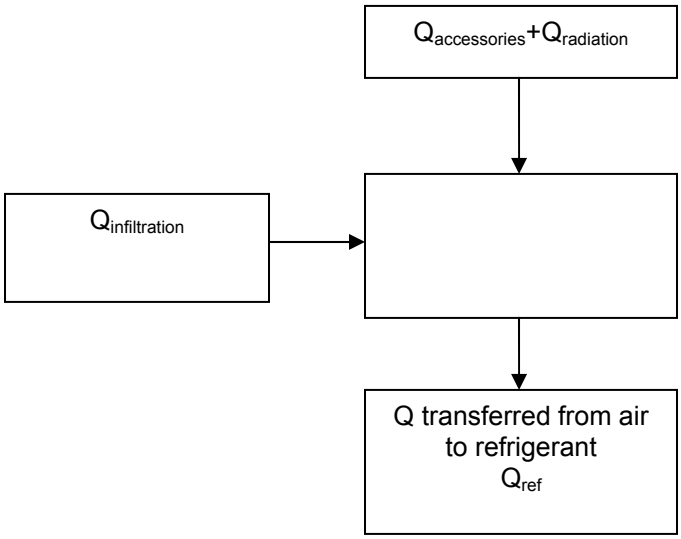

Figure 4.1.1 Schematic showing energy balance for the On-cycle time

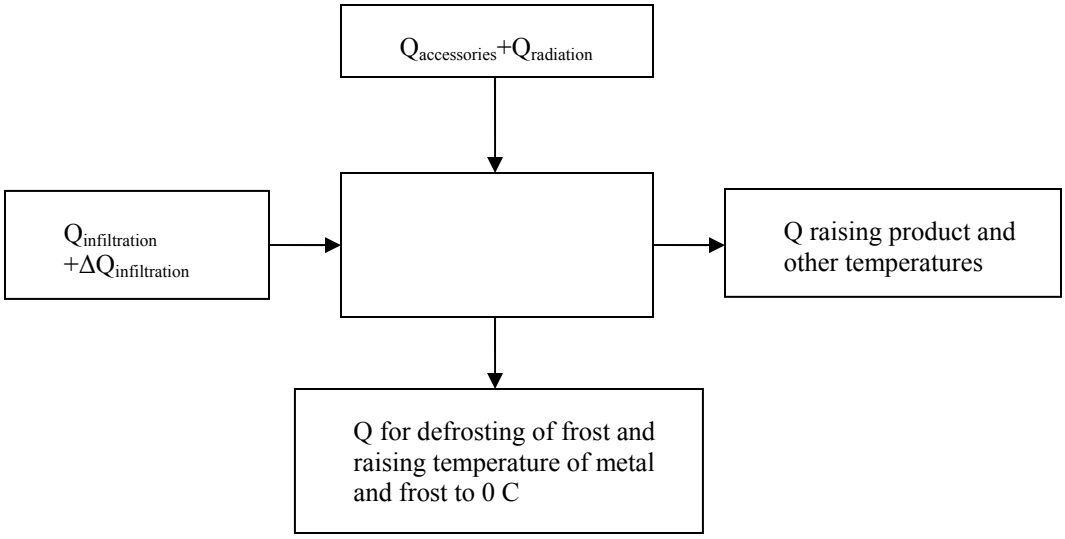

Figure 4.1.2 Schematic showing energy balance for the off-cycle

By considering the schematics for the on and off cycles, we have the following relation,

$$\Delta Q_{\inf} + \left(Q_{accessory,off} + Q_{\inf iltration,steady-state-value} + Q_{radiation,off}\right) = m_{fr} \cdot h_{if} + Q_{pulldown} + C_{frost} \cdot \Delta T_{fr,0} \quad (4.1.2)$$

The second term on the left hand side is numerically equal to the steady state load during the on-cycle. Thus we can estimate the pulldown load. In the above calculations, the load due to the pulldown has to be converted into an energy quantity by factoring in the COP of the system. Since the pulldown load is met exclusively by the compressor, the on-cycle average COP is used for calculating the energy penalty due to the pulldown load

$$COP = \frac{Q_{load-ON}}{W_{compressor}} \quad (4.1.3)$$

Given such a definition of the COP, the possible decrease in evaporating temperature leading to increased compressor power and energy requirement is factored in.

Using equations 4.1.1 to 4.1.3, it is possible to plot the individual components and the total penalty of defrosting. This is presented in Figure 4.1.3.

Figure 4.1.3 shows that the penalty of frosting tends to be very high for short run-times and decreases to a lower value for longer run times. The very broad minimum signifies that the pulldown penalty is significant only for short runtimes. Since the food quality is affected by frequent temperature excursions and marketing considerations call for defrosting at times when customer traffic is low, most display cases are defrosted every 6 hours at the cost of a modest energy penalty. Since the pulldown penalty does not change the comparison significantly, it is sufficient to compare coils by focusing only on the compressor and fan power in the frosted condition (i.e. for a typical runtime).

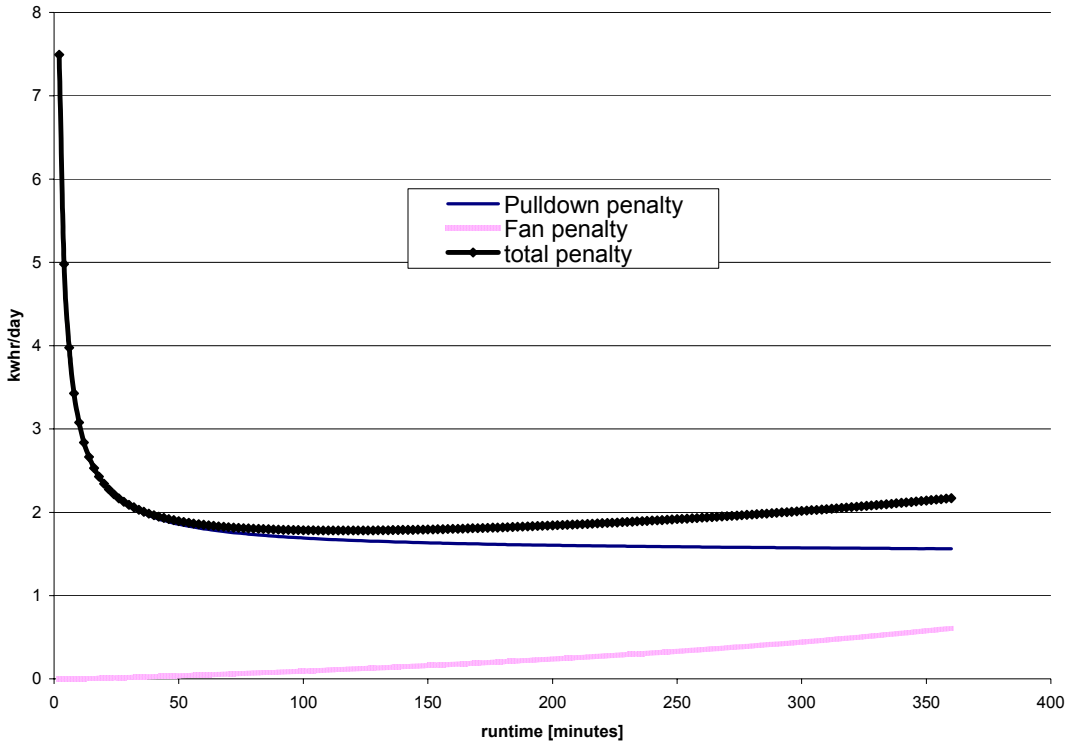

Figure 4.1.3 Energy penalty as a function of run-time

4.2 Parameters in coil design

Most medium temperature display case evaporators are round tube, plain fin type cross counterflow heat exchangers. Apart from this restriction, a few other parameters are limited within logical limits. This section briefly outlines the logic of designing a new coil and the parameter space chosen for the new design.

The efforts to improve performance are directed at

1. Reducing the air-side resistance by increasing the effective (hAair)
2. Reducing the refrigerant-side resistance by focusing on ΔT_{ref} and ΔT_{sat}.
3. Reducing the resistance through the frost.
4. Distributing the frost to maintain uniform free flow area. Nonuniform frosting can result in huge fan power penalties. The uniformity of frosting can be monitored numerically by local pressure drops and total fan power. It is easiest to visualize by plotting the maximum velocities along the airflow direction.

The parameters that can be varied to achieve the above objectives include fin and tube dimensions, materials and circuiting. The range of the parameter space explored is given.

The quantitative results generated by the simulations include fan and compressor power. These are used along with the frost distribution figures to compare coils. It is sufficient to use the compressor and fan power instead of the total energy consumption (which includes the pulldown loads due to defrosting of the coils) because the inclusion of the pulldown penalty does not change the comparison between coils.

Table 4.1 Coil design parameters and their range

No.	Parameter	Range	Notes
COIL PARAMETERS			
1	Tube Diameter	10mm (3/8”) microfinned tubes	Few 8mm tubes also considered
2	Transverse tube spacing	1.25” (31.75mm), 1.5” (38 mm)	
3	Longitudinal tube spacing	1.08” (26mm), 1.3” (33mm)	
4	Transverse tube row no.	4,5,6	
5	Longitudinal tube row no	10,12,15,18	
6	Duct height	5”, 6”, 7.6”	
7	Fin thickness	0.1397 mm (0.0055”) to 0.2413 mm (0.0095”)	Few 0.0105” fins checked
8	Fin density	2 to 7 fpi	
9	Number of modules	2, 3, 4	3 to 9 rows deep
10	Coil width	8 feet	Usual value for display cases
11	Coil depth	0.3m (12”) to 0.48m (19”)	
12	Number of circuits	3, 4, 5, 6, 8	
13	Inter-module spacing	12mm (0.5”)	All coils
14	Tube and fin material	Cu tubes, Al fins	Cu fins: costly
15	Position of coil	Bottom mounted, back mounted	
OPERATING PARAMETERS			
1	Steady state load	4 kW	
2	Discharge air temperature	-1.5 C, -2.5 C	
3	Store conditions	24 C, 55% R.H.	ASHRAE
4	Airflow rate	750 cfm, 700 cfm	Variable speed fans

Chapter 5. Exploring the Parameter Space

This section is presented as the study of a series of changes possible to the parameters listed in Section 4.2. The discussion is limited to the results. The actual physical reasoning is limited to cases where it is not apparent. A note of caution: The coils listed in any single Table have the same flow rate, duct height, load, target DAT, tube diameter, number of modules, infiltration fraction. However two different Tables could differ in one or more of these, hence care must be taken while comparing coils from one Table with a coil from another.

5.1 Effect of changing the tube spacings

The tube spacing in the transverse and longitudinal directions affect the maximum velocities and also the relative tube and fin air side areas. They also influence the refrigerant-side pressure drop and consequently the resistance on the refrigerant side. Here we explore changing the transverse and longitudinal spacing without changing the overall coil dimensions. This is done to understand the effect of spacing alone on performance.

Table 5.1.1 shows the effect of increasing transverse tube spacing from 1.25" to 1.5.

Table 5.1.1 Effect of increasing transverse tube spacing

Duct=7.6", Longitudinal spacing = 1.08", DAT= -1.5 C, 3/8" tubes, 0.0095" Al fins, 6 circuits							
Fin Staging	Transverse Spacing	Tevap	Frost mass	Fin frost	Tube frost	Wcomp	Ideal Wfan
	inches	[C]	[kg]	[m]	[m]	[W]	[W]
3.5 hour runtime							
10 x 6 4@2fpi, 6@4fpi	1.25"	-3.87	6.5	0.00104	0.00146	1016	7.4
10 x 5 4@2fpi, 6@4fpi	1.5"	-4.05	6.43	0.00099	0.00151	1021	6.23

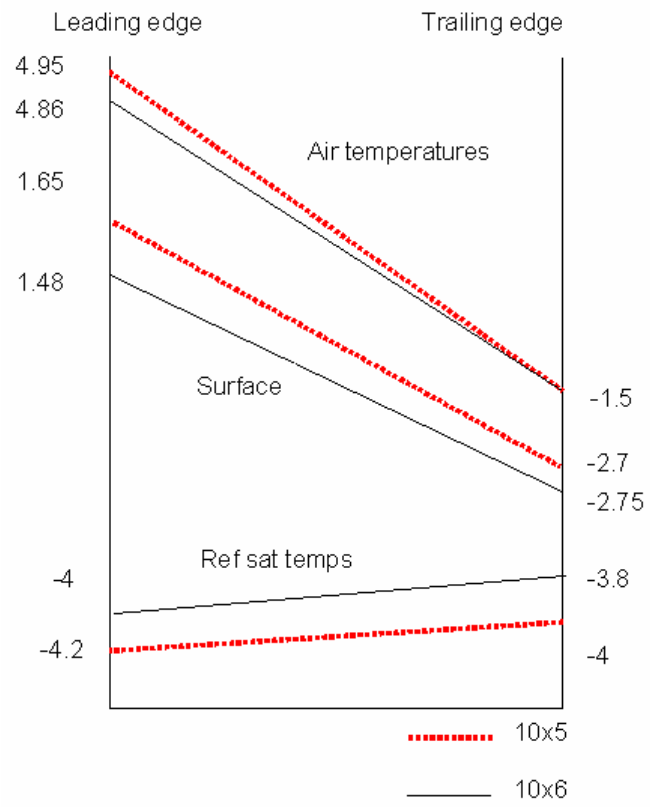

Figure 5.1.1 Temperatures in coils with different transverse tube spacings

An increase in the transverse tube spacing results in a drop in the fin efficiency causing an increased air-side resistance and a consequent drop in evaporating temperature. The advantage of increasing the transverse tube spacing is the reduction in frost formation on the fin and lower maximum velocities resulting in lower fan power requirements. Thus on its own, increasing the transverse tube spacing is beneficial only if the fan efficiencies are low (in this example, the fan has to be less than 26% efficient). But usually the increase in transverse tube spacing is done in conjunction with some other change

The effects of increasing the longitudinal spacing while keeping the depth constant are explored in Table 5.1.2.

Table 5.1.2 Effect of increasing longitudinal tube spacing (same core volume)

Duct=7.6", Transverse spacing = 1.5", DAT= -1.5 C, 3/8" tubes, 0.0095" Al fins, 6 circuits								
Fin Staging	Longitudinal Spacing	Tevap inlet	Tevap outlet	Frost mass	Fin frost	Tube frost	Wcomp	Ideal Wfan
	inches	[C]	[C]	[kg]	[m]	[m]	[W]	[W]
3.5 hour runtime								
12 x 5 4@2fpi, 8@4fpi	1.08"	-3	-3.5	6.39	0.00085	0.00133	999	6.39
10 x 5 4@2fpi, 6@4fpi	1.3"	-3.52	-3.9	6.45	0.00082	0.00136	1011	5.99

When the tube spacing is increased keeping the core volume constant, the lower tube area combines with lower fin efficiency to increase the resistance on the air and refrigerant sides. The small reductions in refrigerant and air-side pressure drops do not make up for the loss in evaporating temperature. Hence an increase in the longitudinal spacing while at constant core volume is not beneficial.

5.2 Increasing air-side area

The most obvious way to decrease air-side resistance is to increase the air-side area. One option is to increase the overall volume of the coil (increasing either the height of the coil or the depth of the coil); another is to increase the fin density.

5.2.1 Increasing core volume

Increasing the core volume allows an increase in the air-side area. The core volume can be increased by making the coils deeper. There are limits placed on the height and depth of the coil in the bottom mounted and back mounted positions. These limits do vary from manufacturer to manufacturer. So this document uses limits based on the leading manufacturers. The limit on the depth of the coil in the bottom mounted position is 14" while the limit on the height is taken to be 7.6". The back mounted coils do not have a set limit on the depth (but there is a limit due to pressure drop as will be clear from further portions of this document), but do have a limit of 6" on the height of the coil. The reader is cautioned regarding the different air flow rates being used for the back mounted and the bottom mounted evaporator coils. The display cases with back mounted coils have a flow rate lower than the bottom mounted ones. The difference arises due to the different construction of the case itself and due to the fact that the thinner back mounted coils will have a very high air-side pressure drop with the original flow rates.

This section explores various ways of increasing the core volume. First the option of increasing the longitudinal spacing along with the depth of the coil is explored. Table 5.2.1.1 compares two coils with different depths and different longitudinal spacings.

Table 5.2.1.1 Coils with different longitudinal tube spacings and different core depths.

Duct=7.6", Transverse spacing = 1.5", DAT= -1.5 C, 3/8" tubes, 0.0095" Al fins, 5 circuits Flow rate=750 cfm					
Fin Staging	Tevap inlet	Tevap outlet	Frost mass	Wcomp	Ideal Wfan
	[C]	[C]	[kg]	[W]	[W]
3.5 hour runtime					
10x5 4@2 6@4 1.08" longitudinal spacing	-3.85	-4.1	6.46	1022	6.2
10x5 4@2 6@4 1.3" longitudinal spacing	-3.52	-3.9	6.45	1011	5.9

Increasing the core depth with an accompanying increase in the core depth increases the evaporating temperatures which results in a drop in compressor and fan power in both the dry and frosted conditions. Thus an increased longitudinal spacing is beneficial from the viewpoint of energy consumption. Further coils presented usually make use of this fact.

Next, the possibility of increasing the depth of the coil even further is explored. As mentioned earlier, coils deeper than a certain limit have to be back mounted and hence have to be shorter compared to bottom mounted coils. The following three Tables illustrate the effect of shifting area from the height to the depth of the coil. Table 5.2.1.2 presents bottom mounted coils while the remaining two Tables present back mounted coils.

Table 5.2.1.2 Twelve row, 7.6” high coils

Duct=7.6", Transverse spacing = 1.5", Longitudinal spacing=1.3" DAT= -2.5 C, 3/8" tubes, 0.0095" Al fins, 6 circuits Flow rate=750 cfm					
Fin Staging	Tevap inlet	Tevap outlet	Frost mass	Wcomp	Ideal Wfan
	[C]	[C]	[kg]	[W]	[W]
6 hour runtime					
12x5 3@3 3@4 6@6	-3.31	-3.8	12.7	1028	13.03
12x5 3@2 5@4 4@5	-3.6	-4.1	12.6	1034	12.42

Tables 5.2.1.2 and 5.2.1.3 show that making a coil deeper at the cost of transverse tube spacing and height leads to a massive increase in the fan power requirement due to the increase in velocities (despite the lower flow rates). The resistances on the air and refrigerant side are comparable (the pressure drop does increase) and hence the compressor powers are not significantly affected.

Table 5.2.1.3 Fifteen row 5” high coils

Duct=5", Transverse spacing = 1.2", Longitudinal spacing=1.3" DAT= -2.5 C, 3/8" tubes, 0.0095" Al fins, 4 circuits Flow rate=700 cfm					
Fin Staging	Tevap inlet	Tevap outlet	Frost mass	Wcomp	Ideal Wfan
	[C]	[C]	[kg]	[W]	[W]
6 hour runtime					
15x4 5@3 5@4 5@5	-3.4	-4.5	12.8	1039	30.6
15x4 5@3 7@4 3@5	-3.4	-4.6	12.9	1041	31

The resistances on the air and refrigerant side are comparable (the pressure drop does increase) and hence the compressor powers are not significantly affected. However given the fact that the fan power is very much higher the approach is not feasible. It is possible to lower the fan power by using a larger transverse spacing between the tubes. Table 5.2.1.4 explores this option for a 5" high coil by increasing the transverse tube spacing for the same core height. To compensate for the loss in tube-side area due to the increase in transverse tube spacing, the coil is made deeper.

The most important effect of increasing the depth to 18 rows is the very large increase in refrigerant pressure drop leading to very low exit refrigerant temperatures. Hence the compressor power requirement is higher. This result implies that increasing the transverse tube spacing without an accompanying increase in coil height is unlikely to improve performance. Also, the refrigerant side pressure drop is the biggest limit to increasing the depth of the coil. However this limit can be overcome by lowering the pressure drop by means discussed in further sections of this document (increasing number of circuits)

Table 5.2.1.4 Eighteen row 5" high coils

Duct=5", Transverse spacing = 1.5", DAT= -2.5 C, Longitudinal tube spacing=1.3" 3/8" tubes, 0.0095" Al fins, 4 circuits Flow rate=700 cfm					
Fin Staging	Tevap inlet	Tevap outlet	Frost mass	Wcomp	Ideal Wfan
	[C]	[C]	[kg]	[W]	[W]
6 hour runtime					
18x3 6@3 6@4 6@6	-2.7	-5.4	13	1067	20.8
18x3 6@2 6@4 6@6	-2.8	-5.9	12.7	1078	19.1
18x3 6@2 6@4 6@6	-2.9	-6.1	12.7	1086	18.6

All the coils presented in Tables 5.2.1.2-5.2.1.4 where the coil height has been reduced, achieve an increase in heat transfer coefficients on the air-side. In some this translates to a reduction in total air-side resistance (after factoring in the efficiencies and the areas). The biggest shortcoming of this method is the accompanying increase in

frictional pressure drop and fan power. To test the possibility of reducing the fan power while continuing to use 15 row coils, a few coils with an extra inch of coil height are tested.

The coils in Table 5.2.1.5 show that increasing the duct height by 1" leads to a substantial lowering of fan and compressor power requirement compared to the 5" high coils. This is mainly due to reducing the pressure drop on the air-side. Also these coils do not suffer the very high refrigerant-side pressure drop associated with the 18 row coils.

Compared with the 12 row coils, these coils show lower fan power requirement (due to lower flow rate), and also a lower evaporating temperature and higher refrigerant pressure drop. One method of improving these is discussed in Section 5.3 by increasing the number of circuits. Another way to improve coil performance is to reduce non-uniformities in the frost distribution (shown in Figure 5.2.1.1 by the dark line). One quick-fix solution is shown by the dashed line. It is possible to sacrifice some efficiency by making the first few rows of thinner fin stock, so the locally warmer fins shift frost to other regions. But this is a non-optimal way and we explore other methods in Section 5.2.2.

Table 5.2.1.5 Fifteen row 6" high coils

Duct=6", Transverse spacing = 1.5", Longitudinal spacing=1.3" DAT= -2.5 C, 3/8" tubes, 0.0095" Al fins, 4 circuits Flow rate=700 cfm					
Fin Staging	Tevap inlet	Tevap outlet	Frost mass	Wcomp	Ideal Wfan
	[C]	[C]	[kg]	[W]	[W]
6 hour runtime					
15x4 5@3 5@4 5@5	-3.25	-4.4	12.9	1034	11.6
15x4 5@3 7@4 3@5	-3.31	-4.5	12.9	1035	11.5

5.2.2 Varying fin density along the length of the coil

Fin density can be varied along the airflow direction to improve the performance. Increasing the fin density increases the air-side area and reduces the air-side resistance. But any increase in the fin density in the front of the coil can increase frost blockage and hence increase the fan power requirement. Thus there is a necessity to distribute fin area such that it is possible to increase fin density without increasing the air-side pressure drop significantly. In other words, it is necessary to maintain uniform free-flow area for the air.

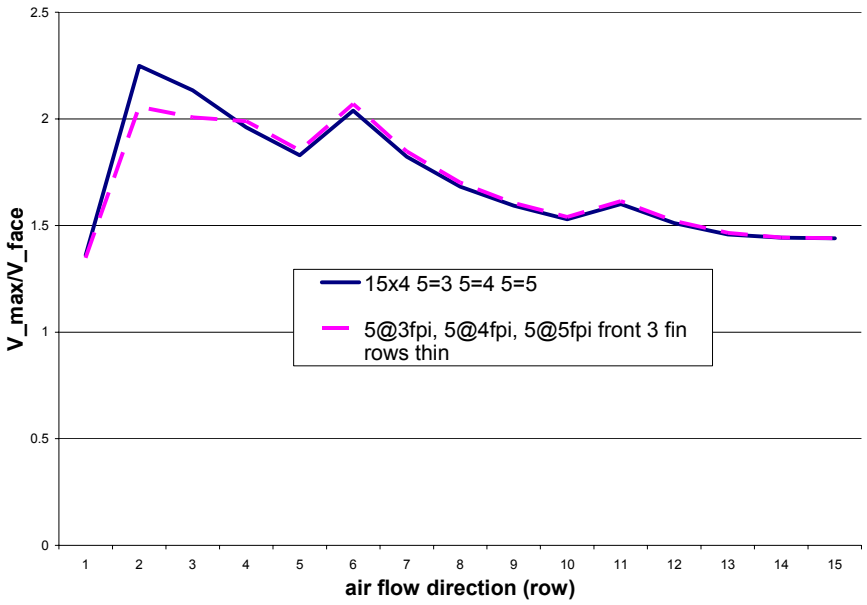

Figure 5.2.1.1 Velocity distribution in 6" high 15 row coils

The possibility of improving the frost distribution focusing on the coils discussed in Table 5.2.1.5. The fin density is lowered in the portion of highest frosting and the fin density at the back of the coil is increased while maintaining the other dimensions and parameters unchanged.

Comparison of the Tables 5.2.2.1 and 5.2.1.5 reveals that "shifting" fin area to the back improves frost distribution leading to lower fan power consumption. Also, the overall refrigerant and air-side resistances are similar and hence the evaporating temperatures at the inlet and exit are similar.

Figure 5.2.2.1 when compared to Figure 5.2.1.1 shows that shifting fin area from the front to the back is a viable alternative to improve the frost distribution.

Now, the possibility of further increasing the fin density at the back (without removing more fin area from the front) is explored. The idea of this exercise is to arrive at the limit for increasing the fin density at the back of the coil. Table 5.2.2.2 and Figure 5.2.2.2 show a limiting case where the same coils as in Table 5.2.2.1 have 7 fpi at the back of the coil.

Table 5.2.2.1 Fifteen row coils of 6” height with lower fin spacing in the front

Duct=6", Transverse spacing = 1.5", Longitudinal tube spacing=1.3" , DAT= -2.5 C 3/8" tubes, 0.0095" Al fins, 4 circuits Flow rate=700 cfm					
Fin Staging	Tevap inlet	Tevap outlet	Frost mass	Wcomp	Ideal Wfan
	[C]	[C]	[kg]	[W]	[W]
6 hour runtime					
15x4 5@2 3@4 7@6	-3.2	-4.5	12.6	1033	11.58
15x4 3@2 4@3 8@6	-3.4	-4.6	12.6	1035	11.2

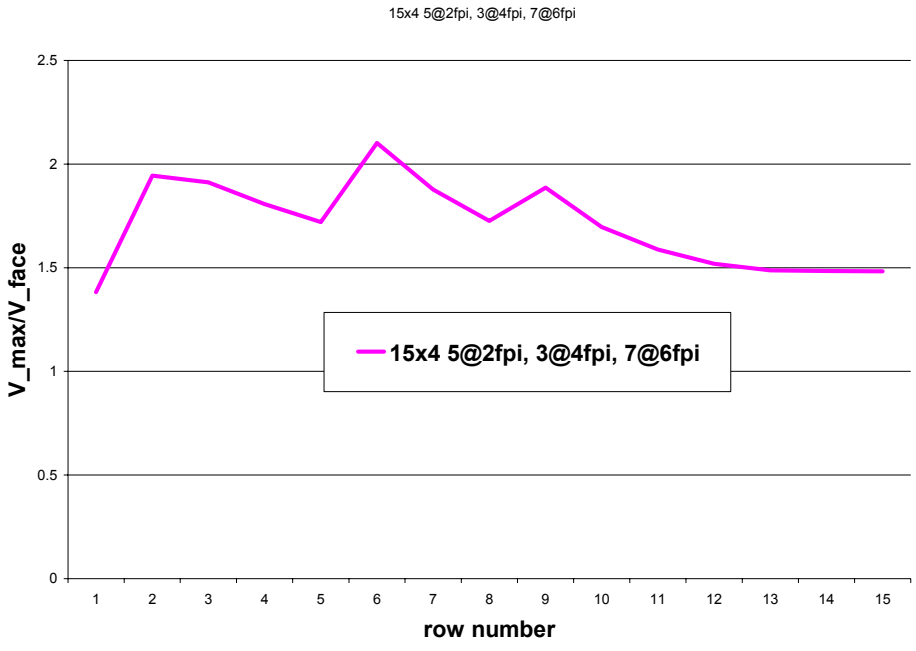

Figure 5.2.2.1 Six inch high coil with lower fin spacing in front

Table 5.2.2.2 Fifteen row coil of 6" height with high fin density at the back

Duct=6", Transverse spacing = 1.5", Longitudinal spacing=1.3" DAT= -2.5 C, 3/8" tubes, 0.0095" Al fins,4 circuits Flow rate=700 cfm					
Fin Staging	Tevap inlet	Tevap outlet	Frost mass	Wcomp	Ideal W fan
	[C]	[C]	[kg]	[W]	[W]
6 hour runtime					
15x4 5@2 3@4 7@7	-3.16	-4.4	12.5	1030	11.8

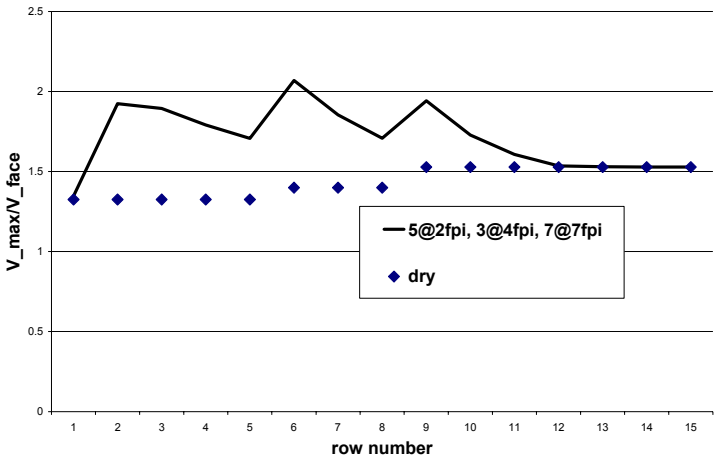

Figure 5.2.2.2 Frost distribution for 6" coil with high fin density at the back

The increase in fin density to 7fpi at the back does raise the evaporating temperature without changing the refrigerant side pressure drop, thus lowering compressor power. Not surprisingly, it also leads to an increase in the fan power requirement. The most significant result of this increase in fin density is inferred from Figure 5.2.2.2. This figure overlays plots of frosted and dry distributions and shows that no frost is deposited after the 12th row. Thus any further increase in fin density at the back will not redistribute the frost from the front to the back. Thus there is a limit to which fin area can be removed from the front modules and placed in the back modules. It must be remembered however that an increase in fin density at the front simultaneously with an increase at the back will change the evaporating temperature, but as seen in Table 5.2.2.2, this will lead to an increase in the fan power requirement. Thus increasing fin density has limits from both the fan power point of view and heat and mass transfer viewpoint.

5.3 Increasing the number of circuits

The number of circuits determines the refrigerant mass flux and thus governs the refrigerant side heat transfer and pressure drop tradeoffs. Thus increasing the number of circuits offers a method of improving performance by lowering the refrigerant side pressure drop. The effect on temperatures and resistances is outlined in Figure 5.3.1.

Changing the number of circuits has the effect of reducing the refrigerant pressure drop while at the same time reducing the refrigerant side heat transfer coefficient. These effects are borne out by Figure 5.3.1. The inlet evaporating temperatures are lower due to the higher resistance on the refrigerant side.

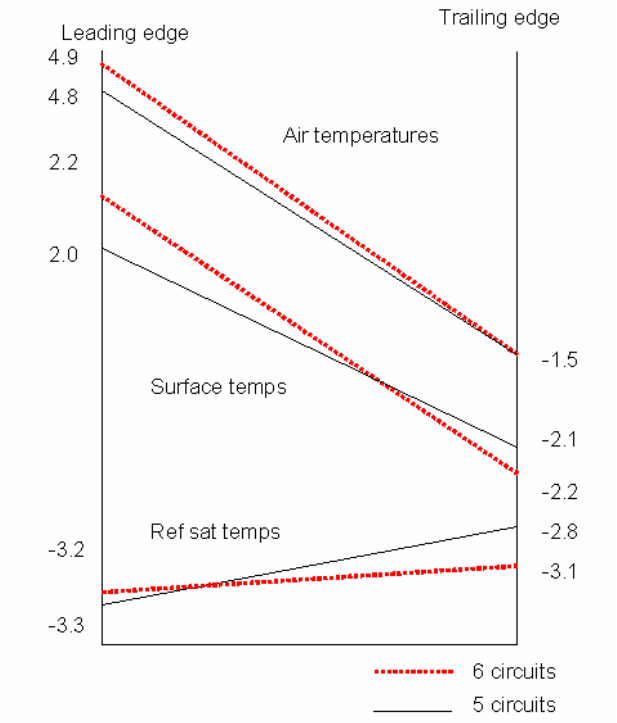

Figure 5.3.1 Comparison of two 12x5 coils with different number of circuits

The reduction in pressure drop by increasing the number of circuits results in a higher exit temperature for the refrigerant. This leads to warmer surfaces at the leading edge, thus reducing the frosting at the leading edge and improving the frost distribution.

Thus, increasing the number of circuits is an effective way of improving the performance of an evaporator despite the increase in heat transfer resistance. This is mainly due to the lower drop in refrigerant temperature from inlet to exit. Thus, it serves as a method of improving the performance of coils which have high compressor power requirements on account of a high refrigerant side pressure drop. The use of this method is illustrated in later sections of this document.

5.4 Lowering tube diameters

Lowering the tube diameter reduces the refrigerant side resistance. But at the same time, there is an increase in refrigerant side pressure drop. Hence there is a necessity to simultaneously increase the number of

circuits as discussed in the earlier section. Table 5.4.1 presents coils with 8mm diameter Cu tubes with 0.00105" thick fins. Lower tube diameters lead to lower fin efficiency for the same tube spacings. Hence when lower tube diameters are considered, it is necessary to also use thicker fins to adjust for the loss in efficiency.

Table 5.4.1 shows that the increase in inlet evaporating temperature is offset by refrigerant side pressure drop leading to lower evaporating temperature at the exit and hence leading to more leading edge frosting and consequently higher fan power requirement. Once the number of circuits is increased, there is a small penalty in the inlet evaporating temperature, but this is offset by the reduction in the refrigerant side pressure drop. Thus any reduction in tube diameter from the current 9.525 mm (3/8") necessitates an increase in fin thickness and also in the number of circuits.

Thus Section 5 outlined various ways to achieve the 4 objectives listed in Section 4.3. In short, increasing fin density at the back to a limit of ~6fpi, using a larger number of circuits helped reduce the air and refrigerant side resistances. Smaller tube diameters with thicker fins do not appear to be beneficial. Frost distribution can be improved by selecting the number of circuits to keep the refrigerant saturation temperature drop as low as possible and increasing the transverse and longitudinal tube spacings. These general guidelines are used to develop coils for specific applications in Section 6. Section 6 emphasizes results and the reasons are outlined in Section 5.

Table 5.4.1 Fifteen rows of 8mm tubes based coils of 6" height.

Duct=6", Transverse spacing = 1.5", Longitudinal spacing=1.3" DAT= -2.5 C, 8mm tubes, 0.0105" Al fins, 6 circuits Flow rate=700 cfm					
Fin Staging	Tevap inlet	Tevap outlet	Frost mass	Wcomp	Ideal Wfan
	[C]	[C]	[kg]	[W]	[W]
6 hour runtime					
15x4 3@2 4@3 8@6	-3.7	-4.5	12.5	1031	10.2
15x4 5@2 3@4 7@6	-3.3	-4.4	12.5	1030	10.25

Chapter 6. Results: Coil Design for Given Core Volume

This section uses the results from Section 5 to design evaporators for given volume restrictions. The first of the two coils designed here has additional restrictions on the tube and fin sizes and spacings. The second coil developed here only has volume restrictions.

The following manufacturing constraints were considered while selecting a coil for Prototype-2.

1. The maximum tube spacing available is 3.175 cm (1.25") in the transverse and 2.7 cm (1.08") in the longitudinal direction (same as the existing copper prototype now in case)
2. The fins available are 0.1397 mm (0.0055"), 0.1905mm (0.0075") and 0.2413mm (0.0095") thick
3. The available core dimensions are 0.193*2.057*0.343 m (75/8*81*13.5")
4. The number of rows in the airflow direction is restricted to even numbers (e.g. 10 or 12)

A few of the many coil designs considered are presented in Table 6.1. Larger number of circuits was not considered for this prototype due to circuiting issues and the number was restricted to the number of transverse tube rows. The last coil presented in Table 6.1 was chosen to be Prototype-2.

The reasons for the choice were the more uniform frosting of the coil and the lower energy consumption. The fin densities were kept to a much lower limit (4fpi at the back) given the restriction on the tube spacings. A higher fin density would have been employed if there was the liberty to either have a deeper coil or a coil with higher tube spacings. The testing of the Prototype-2 coil confirmed the advantages of the steps taken

Table 6.1 Comparison of coils designed with manufacturing restrictions

Duct=7.6", Transverse spacing = 1.25", Longitudinal spacing=1.083" DAT= -2.5 C, 3/8" tubes, Al fins, 6 circuits Flow rate=750 cfm					
Fin Staging	Tevap inlet	Tevap outlet	Frost mass	Wcomp	Ideal Wfan
	[C]	[C]	[kg]	[W]	[W]
6 hour runtime					
10x6 4@2 6@4	-4.9	-5.1	12.7	1068	19.3
10x6 4@3 6@4 0.0055" fins at the front	-4.6	-4.8	12.8	1058	16.3
12x6 5@3 7@4 0.0055" fins at the front	-4	-4.4	12.7	1045	13
12x6 6@3 6@4 0.0055" fins at the front	-4.1	-4.4	12.7	1047	14.4
12x6 5@3 7@4 0.0095" fins throughout	-3.9	-4.3	12.7	1043	12.7

SCE reported that the compressor energy usage for a day dropped by 28% and that the system EER increased by 35% when compared to the original Hill Phoenix display case).

As a final exercise, the restrictions on the depth of the coil and inter-tube spacings placed while developing Prototype-2 are removed. The resulting coil was developed as a continuation of the coils presented in Section 5. Two coils with low energy consumption and a pretty uniform frost distribution are shown in Table 6.2.

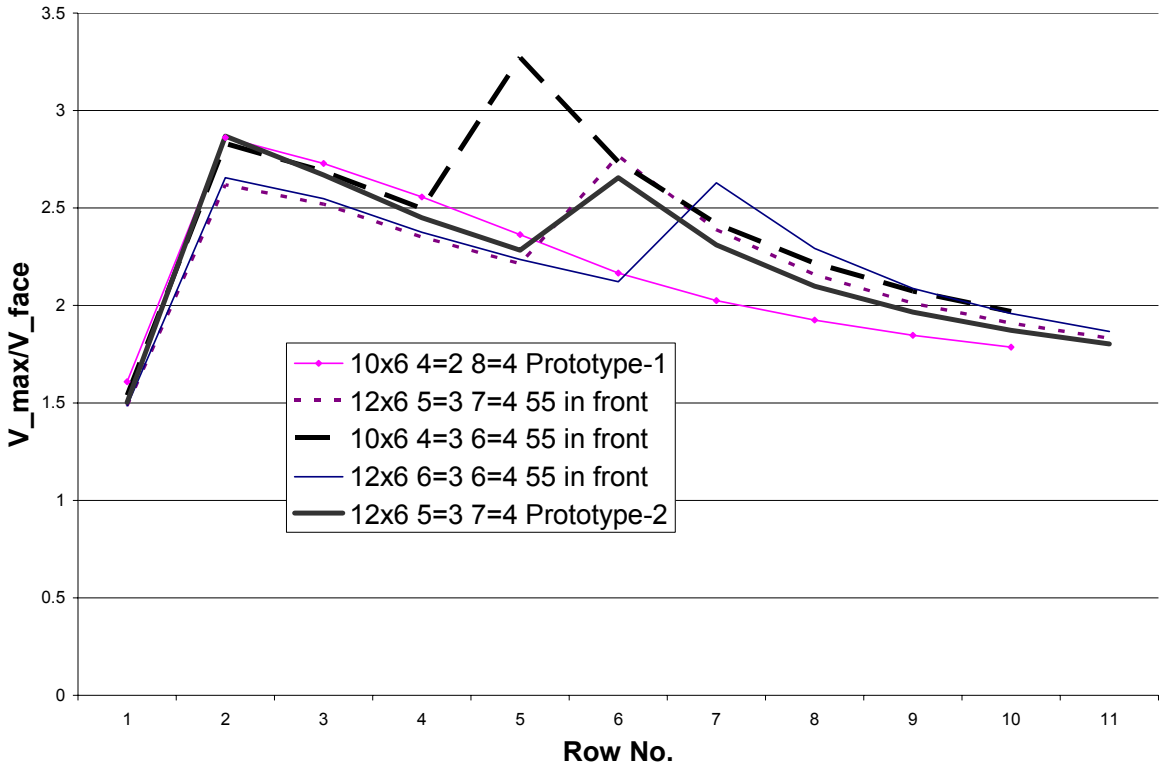

Figure 6.1 Velocity distribution of coils considered for Prototype-2

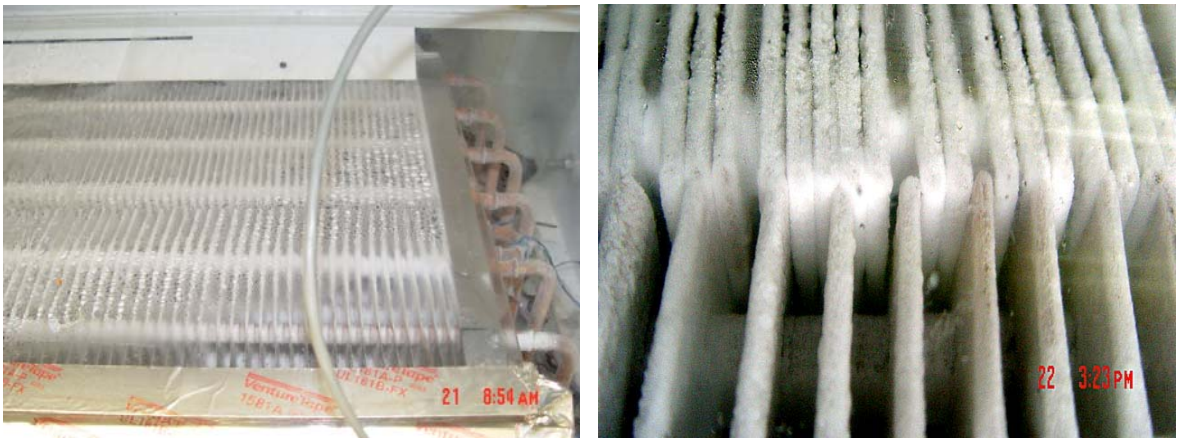

Figure 6.2 Prototype-2(left) versus Prototype-1(right)

Table 6.2 Coils with manufacturing restrictions removed

Duct=6", Transverse spacing = 1.5", Longitudinal spacing=1.3" DAT= -2.5 C, 3/8" tubes, 0.0095" Al fins, 6 circuits Flow rate=700 cfm					
Fin Staging	Tevap inlet	Tevap outlet	Frost mass	Wcomp	Ideal Wfan
	[C]	[C]	[kg]	[W]	[W]
6 hour runtime					
15x4 3@2 4@3 8@6	-3.7	-4	12.5	1020	10.8
15x4 5@2 3@4 7@6	-3.6	-3.95	12.4	1015	11

As seen from Table 6.2, 6.1, and those in Section 5.2.2, the coils presented here achieve a lower refrigerant side pressure drop while not losing out on refrigerant side heat transfer. Also, the fin densities are not larger than required (Figure 6.3 shows that the coils do not asymptote to a flat line) and hence the back portions too participate in the heat and mass transfer.

The coils developed in Table 6.2 are more ambitious than Prototype-2 in terms of cost and have not been built. But the fact that Prototype-2 did lead to benefits suggests that these 2 coils too will prove beneficial in terms of efficient operation. Cost factors are not within the scope of this publication and will be a key factor in choosing coils. Nonetheless, the methodology presented here can be used to design coils with any restrictions as was shown in the development of Prototype-2.

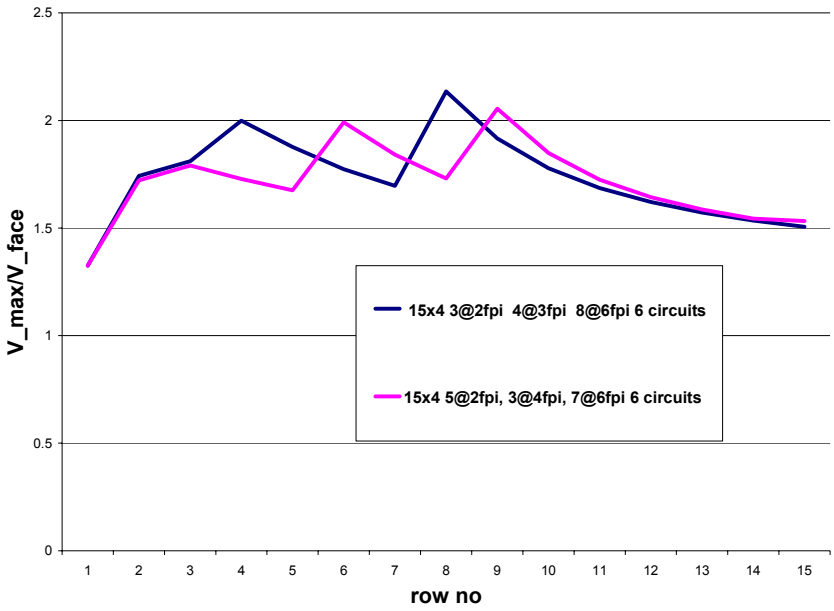

Figure 6.3 Coils manufactured without depth and tube spacing restrictions

Chapter 7. Conclusions and Recommendations

This report described further development, validation and use of a simulation model for designing efficient evaporators for display cases. The model had been developed earlier from an extensive set of experiments in an evaporator calorimeter under frosting conditions.

The evaporator simulation model was augmented by equations dealing with duct pressure losses, entrainment of warm moist air into the air curtain and other factors that enabled analysis of feedback effects of frosting (e.g. via fan response) on overall system performance.

This project also extended the validation effort using data from two different evaporators installed in an extensively-instrumented display case. Results showed that the model is capable of accurately predicting trends in air-side and refrigerant-side performance. Comparison of absolute values of some variables was limited by the lack of reliable air flow and pressure drop measurements.

The design tool was used to design a new coil for the display case. The improvement in performance of the new coil (Prototype-2) over the baseline (commercial) coil and is shown in Table 7.1. Prototype 2 was constrained by the availability of existing tube and fin geometries that could be obtained quickly. The design tool was further used to investigate deeper coils which can be mounted in thinner ducts in the back wall of the display case. These and other simulations aimed to optimize designs without restrictions on the tube sizes and spacings. The resulting coils were presented in Section 6.2. Table 7.1 also summarizes results of those simulations, showing an 8-10% reduction in energy consumption compared to Prototype 2, and 15-20% reduction relative to the original baseline coil (assuming 20% fan/motor efficiency).

The lower energy consumption is due primarily to two design changes. First, a significant increase in the refrigerant evaporating temperature was achieved by reducing tube diameter and increasing air-side area. Second, the fan power was controlled by staging the fins to minimize their effect on pressure drop and to achieve a more uniform frost deposition pattern to avoid early blockage near the front of the coil.

Table 7.1 Comparison of Prototype-2, baseline and newer improved prototypes

DAT=-2.5 C 7.6” duct 1.08” longitudinal spacing 1.25” transverse					
Fin Staging	Tevap inlet	Tevap outlet	Frost mass	Wcomp	Ideal Wfan
BASELINE 12x4 12@2fpi 0.5” tube	-8.6	-8.7	12.3	1191	14
PROTOTYPE-2 12x6 5@3fpi 7@4fpi 3/8” tube	-4.1	-4.4	12.7	1093	13.5
DAT=-2.5 C Duct=6”, Transverse spacing = 1.5”, Longitudinal spacing=1.3” 3/8” tubes, 0.0095” Al fins, 6 circuits					
15x4 3@2 4@3 8@6	-3.7	-4	12.5	1020	10.8
15x4 5@2 3@4 7@6	-3.5	-3.9	12.4	1015	11

The last two designs illustrate several important conclusions. The ability to increase energy efficiency by increasing the evaporating temperature is inherently limited by the design requirement to meet a specified discharge

air temperature: -2.5 C in this example. The 1 C approach temperature differences achieved by the proposed coils are at or beyond the practical limit achievable, considering material costs and packaging constraints.

Increasing air-side area by employing higher fin densities has the disadvantage of increased cost. A complete cost analysis is beyond the scope of this project because it is difficult to quantify some of the tradeoffs (e.g. increasing fin densities can actually reduce labor cost by enabling automated assembly). Therefore incremental mass was used as a crude surrogate for incremental cost. For example the original baseline coil had 25 lb of aluminum fins and 17 lb of copper tubes. Assuming a nominal cost of $1/pound of aluminum fin stock, and $2/lb for copper tubes, the material costs for Prototype 2 would be about 70% higher, and the material costs of the improved coils in Table 7.1 would be about 90% greater than the baseline. If assembly costs are relatively insensitive to such changes in coil size and geometry, these incremental (~$40 to $50) costs may be an acceptable option for achieving 20-30% efficiency improvement in a case that consumes electricity costing $500-1000/yr. However, recognizing that the first additions of coil surface area are far more cost-effective than the last, and given the importance of first costs in the HVAC&R industry, it is important to investigate other ways to lower energy consumption of the display case as a whole. The following paragraphs offer some suggestions.

The current project did not investigate flat tubes, fin surface enhancements or other ways of improving fin and/or tube geometries. Whatever the improvements, they are unlikely to improve the performance much beyond what is obtained by the improved coils presented in this document. Flat tubes could help increase evaporating temperature slightly by adding refrigerant-side area to reduce heat transfer resistance, but their greatest advantage could result from reducing fan power and extending runtimes. There is little experience with fin surface enhancements that can tolerate frosting, and existing display cases have fin pitch too high to benefit from wavy fins. However wavy fins are widely used on a/c evaporators because they tolerate condensate well and drain easily, so high fin densities explored here may warrant exploration of wavy fin designs in the downwind modules where fin pitch is small enough to trigger the enhancement mechanism (periodic flow separation and reattachment).

A simple sensitivity analysis was performed on the baseline and the improved coils to explore the feasibility of lowering system energy consumption by reducing the load, focusing on infiltration alone. As has been mentioned earlier, infiltration is responsible for 70% of the sensible load and almost the entire latent load. When the infiltration rate was lowered by 30% (arbitrary value), total power consumption was reduced by 22-25%. This, combined with the fact that improving coil design alone reaches a point of diminishing returns suggests that efforts to improve the air curtain and lower the total infiltration are a necessity. The reduction in infiltration, while holding the DAT constant causes a reduction in the evaporator air inlet temperature. In spite of this, the reduction in sensible and latent load allows the evaporating temperature to increase, leading to compressor power savings and also less frost formation.

Further improvements in display case energy efficiency is possible by be obtained by redesigning the air curtain and back-panel air flow patterns to enable operation at a higher discharge air temperature. Allowing more air to flow through the back panel could improve the heat transfer from the products to the air leading to the possibility of increasing the DAT and hence the evaporating temperature. Such improvements may prove to be more cost-effective than attempting to increase evaporator size and complexity.

Bibliography

Carlson, D. M., P. S. Hrnjak, and C. W. Bullard, 2001. Deposition, distribution, and effects of frost on a multi-row heat exchanger performance. Air Conditioning and Refrigeration Center, University of Illinois at Urbana-Champaign, Report IL TR-183.

Chen, H., L. Thomas, and R. W. Besant, 2000. Modeling frost characteristics on heat exchanger fins: Pt. I, Numerical Model. *ASHRAE Transactions* Vol. 106, Pt.2.

Chen, H., L. Thomas, and R. W. Besant, 2000. Modeling frost characteristics on heat exchanger fins: Pt. II, Model Validation and Limitations. *ASHRAE Transactions* Vol. 106, Pt. 2.

Churchill, S. W., 1977. Friction-factor equation spans all fluid-flow regimes. *Chemical Engineering,* pp. 91-92.

Faramarzi, R., 2003. Experimental data from display case experiments. Personal Communication.

Gnielinski, V, 1976. New equations for heat and mass transfer in turbulent pipe and channel flow. *Chemical Engineering*, 16:359-368.

Granryd, E., E. Ingvar, P. Lundqvist, A. Melinder, B. Palm, and P. Rohlin. 1999. Refrigeration and Engineering, Department of Engineering Technology, Division of Applied Thermodynamics and Refrigeration, Royal Institute of Technology, KTH, Stockholm.

Hayashi, Y., K. Aoki, and H. Yuhura. 1976. Study of frost formation based on a theoretical model of the frost layer. *Trans. Japan Society Mechanical Engineers* Vol. 40 pp. 885-899.

Hayashi, Y., A. Aoki, S. Adachi, and K. Hori. 1977. Study of frost properties correlation with frost formation types. *Journal of Heat Transfer,* Vol. 99, pp. 239-245.

Hoke, J. L., J. G. Georgiadis, and A. M. Jacobi. 2000. The Interaction between the Substrate and Frost Layer through Condensate distribution. PhD Thesis. Dissertation. University of Illinois at Urbana-Champaign.

Jones, B. W. and J. D. Parker. 1975. Frost formation with varying environmental parameters. *Trans. Journal of Heat Transfer,* Vol. 97(2), pp. 255-259.

Kim, N. H., B. Youn, and R. L. Webb. 1999. Air-side heat transfer and friction correlations for plain fin-and-tube heat exchangers with staggered tube arrangements. *Transactions of ASME,* Vol. 121, pp. 662-667.

Klein S. and F. Alvarado, 1995, Engineering Equation Solver, F-Chart Software, Middletown, WI.

Kondepudi, S. N. and D. L. O'Neal. 1987. The effect of frost growth on extended surface heat exchanger performance—a review. *ASHRAE Transactions,* Vol. 93(2), pp. 258-274.

Kondepudi, S.N. and D. L. O'Neal. 1990. The effects of different fin configurations on the performance of finned-tube heat exchangers under frosting conditions. *ASHRAE Transactions,* Vol. 96(2).

Mao Y., R. W. Besant, and H. Chen. 1999. Frost characteristics and heat transfer on a flat plate under freezer operating conditions: Pt. I, experimentation and correlations. *ASHRAE Transactions,* Vol. 105(2), pp. 231-251.

Neshan, 2003, Prototype-1 Design, Personal Communication

Ogawa, K., N. Tanaka, and M. Takeshita. 1993. Performance improvement of plate fin-and-tube heat exchangers under frosting conditions. *ASHRAE Transactions,* Vol. 99, pp. 762-771.

O'Neal, D. L. and D. R. Tree. 1985. A review of frost formation in simple geometries. *ASHRAE Transactions,* Vol. 91, pp. 267-281.

Ostin, R. and S. Andersson. 1991. Frost growth parameters in a forced air stream. *International. Journal of Heat Mass Transfer* Vol. 34, pp. 1009-1017.

Padki, M. M., S. A. Sherif, and R. M. Nelson. 1989. A simple method for modeling the frost formation phenomenon in different geometries. *ASHRAE Transactions,* Vol. 95, pp. 1127-1137.

Raju, S. P. and S. A. Sherif. 1993. Frost formation and heat transfer on circular cylinders in cross-Flow. *International Journal of Refrigeration,* Vol. 16(3), pp. 390-402

Rite, R. W. and R. R. Crawford. 1990. The effect of frosting on the performance of domestic refrigerator-freezer finned tube evaporator coils. Air Conditioning and Refrigeration Center, University of Illinois at Urbana-Champaign, IL. Report TR-01.

Sanders C., 1974. Frost formation: The influence of frost formation and defrosting on the performance of air coolers. Ph.D. Thesis. Technique Hogeschool, Delft, Netherlands.

Senshu, T., H. Yasuday, K. Oguni, and K. Ishibane. 1990. Heat pump performance under frosting conditions Part 1 and 2. *ASHRAE Transactions,* Vol. 96 (1), pp. 324-336.

Souza A. L. and M. M. Pimenta. 1995. Prediction of pressure drop during horizontal two-phase flow of pure and mixed refrigerants. *ASME Conf. Cavitation and Multiphase Flow,* Vol. 210, pp. 161-171.

Storey, B. D. and A. M. Jacobi. 1999. The effect of streamwise vortices on the frost growth rate in developing laminar channel flows. *International Journal of Heat and Mass Transfer,* Vol. 42, pp. 3787-3802.

Tassau, S. A. and D. Datta. 1999. Influence of supermarket environmental parameters on the frosting and defrosting of vertical multideck display cabinets. *ASHRAE Transactions,* Vol. 105(1), pp. 491-496.

Tao, Y.X., R. W. Besant, and K. S. Rezkallah. 1993. A mathematical model for predicting the densification and growth of frost on a flat plate. *International Journal of Heat and Mass Transfer,* Vol. 36(2), pp. 353-363.

Verma P., D. M. Carlson, Y. Wu, C. W. Bullard, and P. S. Hrnjak. 2002. Experimentally validated model for frosting of plain-fin-round-tube heat exchanger. IIR Conference, "New Technologies in Commercial Refrigeration".

Wang, C. C., Y. J. Chang, Y. C. Hsieh, and Y. T. Lin. 1996. Sensible heat and friction characteristics of plate fin-and-tube heat exchangers having plane fins. *International Journal of Refrigeration,* Vol. 19(4), pp. 223-230.

Wang, C. C. and C. T. Chang. 1998. Heat and mass transfer for plate fin-and-tube heat exchangers, with and without hydrophilic coating. *International Journal Heat and Mass Transfer,* Vol. 41, pp. 3109-3120.

Wang, C. C., K. Y. Chi, and C. J. Chang. 2000. Heat transfer and friction characteristics of plain fin-and-tube heat exchangers, Part II: correlation. *International Journal of Heat and Mass Transfer,* Vol. 43(15), pp. 2693-2700.

Wattelet, J. P. and J. C. Chato. 1994. Heat transfer flow regimes of refrigerants in a horizontal-tube evaporator. Air Conditioning and Refrigeration Center, University of Illinois at Urbana-Champaign, IL, Report TR-55.

Watters, R. J., D. L. O'Neal, and J. Yang. 2002. Frost/defrost performance of a three-row fin staged heat pump evaporator. *ASHRAE Transactions,* Vol. 108(2), pp. 353-363.

Verma P., D. M. Carlson, Y. Wu, C. W. Bullard, and P. S. Hrnjak. 2001. Simulating the performance of a heat exchanger during frosting. Air Conditioning and Refrigeration Center, University of Illinois at Urbana-Champaign, Report TR-186.

Yonko, J. D. and. C. F. Sepsy. 1967. An investigation of the thermal conductivity of frost while forming on a flat horizontal plate. *ASHRAE Transactions,* Vol. 73(II), pp. I.1.1-I.1.11.

Appendix A. Details of Validation

A.1 Available measurements and associated issues

The following is an abbreviated list of the data streams available.

1. Evaporator air temperatures → RTDs at the left, center and right (total 3) after the fan. An additional "high quality" measurement at the left section of the coil also provided an air inlet temperature. Similar measurements at the exit of the evaporator
2. Evaporator tube surface temperature→ There are 12 surface thermocouples distributed at the entry, exit and middle of the evaporator to approximate the refrigerant temperature.
3. Refrigerant temperature and pressure → The refrigerant temperature and pressure are measured at the inlet to the TXV and at the exit of the coil. Refrigerant temperatures are also available after the receiver, entry to the display case, etc. These refrigerant temperatures are immersion readings.
4. DAG and RAG measurements → The main parameters available at the DAG and the RAG are the velocities, the temperatures and the relative humidities.
5. Accessory power requirements → The power requirements for the lights, anti-sweat heaters (if in use) are available.
6. Air-side pressure drop etc → Apart from the fan and evaporator pressure drop, actual fan power required is available
7. Product temperatures → Thermocouple readings for the simulated products in the various shelves were measured.
8. Frost → Frost mass is available at the end of each refrigeration period. This is deduced from the amount of condensate collected during the defrosting following the refrigeration period. Frost mass is not available as a function of time. No measurements exist for the frost thickness. A few photographs are available for the 22nd August data set. These give some idea of the frost distribution and thickness.
9. Miscellaneous → Condenser inlet and exit temperature readings, case humidities, room humidities and temperatures.

A few relevant data streams are described below. The aim of presenting these measurements is to show the nature of the measurements and the system. The model does not simulate nonuniform distribution of air/frost perpendicular to the airflow direction. Given this nature of the simulation code, it is necessary to arrive at a single value for those variables that are used as input to the simulation. The following descriptions address this issue.

A.1.1 Temperature of the air at the evaporator inlet

RTD based measurements provide the air temperature at the entry plane of the evaporator coil. The temperatures were measured at the left, right and center of the entry plane. These measurements are shown for the Hill Phoenix coil.

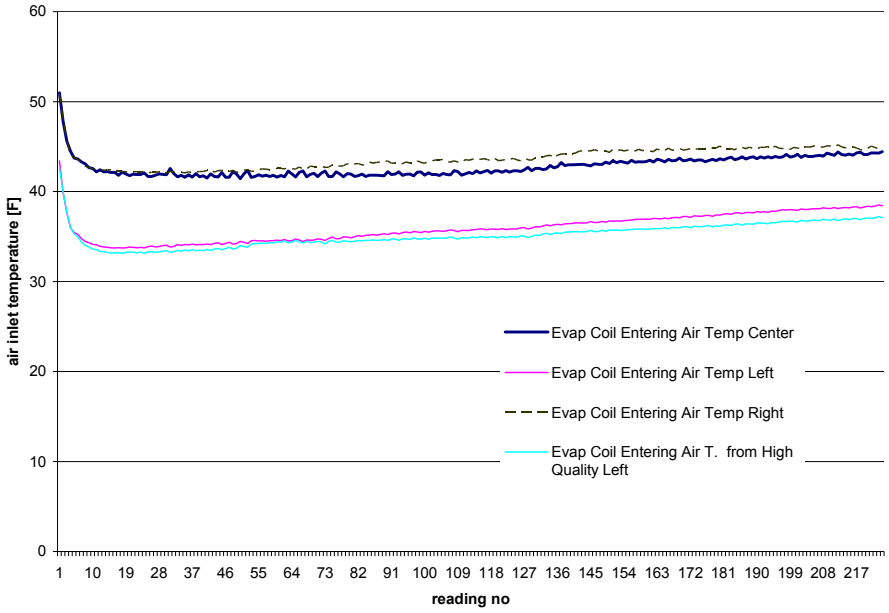

Figure A.1 Hill Phoenix baseline coil air inlet temperature

The above measurements of air inlet temperature show a nonuniform temperature distribution for the air entering the evaporator coil. The air entering at the left side of the plane is obviously much cooler than the air at the center or the right side. The possibility of faulty equipment can be ruled out given the consistency of this observation in all the available data sets. Due to the non-availability of reliable air velocities and distribution data, the air inlet temperatures used as an input are the arithmetic averages of the available readings.

A.1.2 Refrigerant inlet condition

The data sets provided by Southern California Edison include values for the refrigerant temperature and pressure at the inlet to the TXV and the inlet to the evaporator. It is possible to calculate the refrigerant enthalpy at the inlet to the evaporator using the TXV inlet temperature and pressure readings and assuming adiabatic conditions to exist from the TXV outlet to the evaporator inlet.

The refrigerant at the TXV exit is 2-phase (shown in Fig A.2) and the quality is not known directly. It can be determined from the enthalpy and the pressure. The refrigerant temperature at the inlet to the coil is not a meaningful quantity to use as an input to the simulation given the 2-phase nature of the refrigerant at the inlet. The pressure that is measured at the TXV outlet can be used, but there is the possibility of a significant (and unquantifiable) pressure drop from the TXV outlet to the evaporator inlet. In the given data sets, pressure at the outlet of the coil is available. Hence this pressure value is used instead of the pressure at the TXV outlet.

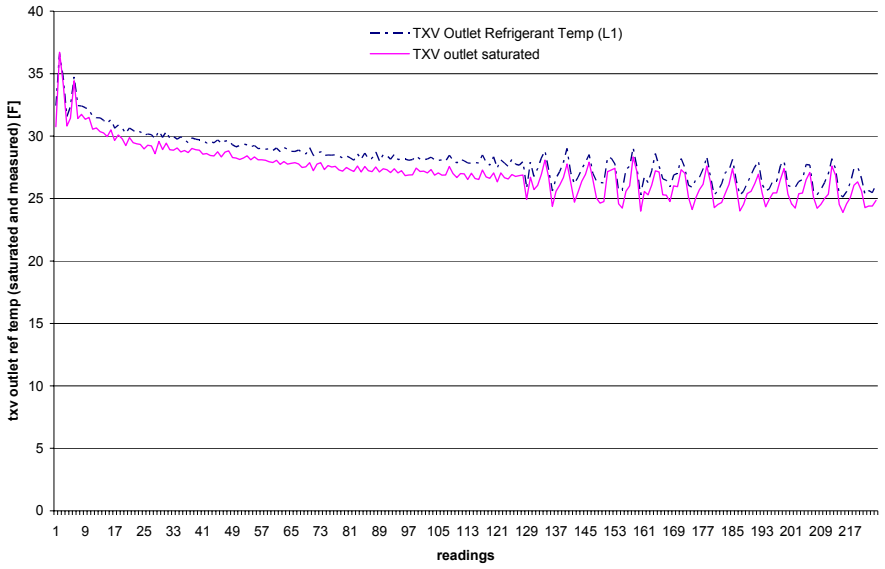

Figure A.2 Comparison of TXV outlet temperature and saturation temperature corresponding to TXV outlet pressure

Thus the refrigerant inlet condition is given by the inlet enthalpy which is calculated from the TXV inlet temperature and pressure. This is necessitated by the lack of alternate data at the evaporator inlet that can be used to calculate the enthalpy of the refrigerant.

A.1.3 Refrigerant surface temperature measurements

Twelve surface thermocouples (4 per plane) give the surface temperature of the coil at the inlet section, middle of the coil and the exit section of the coil. In the original Hill Phoenix coil, there were 4 circuits and each of the 4 circuits had one thermocouple attached to it whereas in the Prototype-1 coil tests, the same number of thermocouples per plane was divided among the 6 circuits.

The surface thermocouple readings provide good clues regarding the heat transfer resistance on the refrigerant side and combined with the model, it can be used to find heat transfer resistance through the frost and the air. Figure A3 shows the coil surface thermocouple readings.

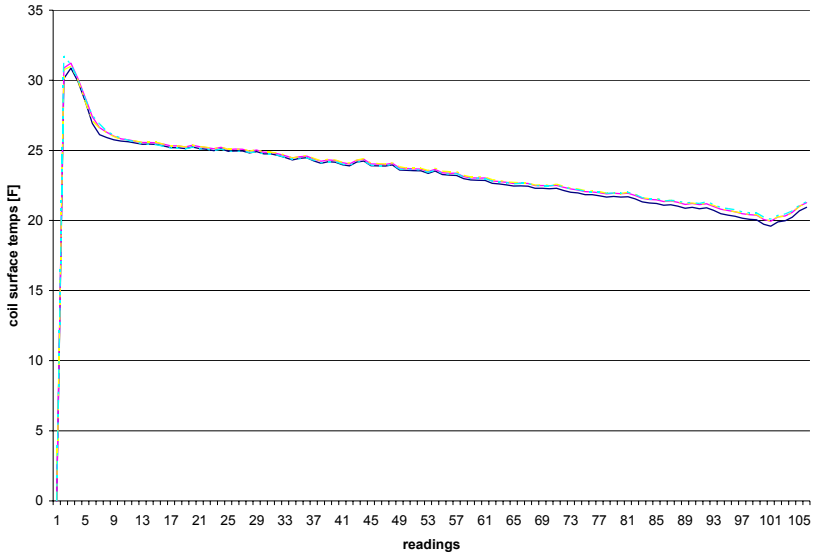

Figure A.3 Coil surface temperatures

The very small difference between the surface temperature readings from one circuit to another allows us to justify an important assumption. All the 6 circuits have identical refrigerant and air-side properties, i.e. the air, refrigerant and frost related variables have unique values at any given plane of the coil and this value does not vary among circuits.

A.1.4 Air inlet humidity

There are only two measurements available for the air inlet humidity. There is a grid measurement of the dew point and there is a high accuracy dew point meter at the left of the coil. Ideally, the grid measurement should provide a more representative measurement of coil inlet humidity, but in two data sets the grid measurements showed erratic behavior, so the only option was to use the dew point measurement at the left end of the inlet plane. Given the non-uniform distribution of the airflow through the coil it is possible that the air inlet dew-point measurement is not a representative one. But any major errors introduced due to this unavailability of the grid reading should not be introduced in the other 4 data sets.

A.1.5 Air outlet temperature and humidity

The placement of the RTDs at the outlet of the coil is similar to that at the inlet to the coil. There are 4 readings, two at the left, one each at the right and the center of the exit plane. Figure A.4 shows the measurements for Prototype-1.

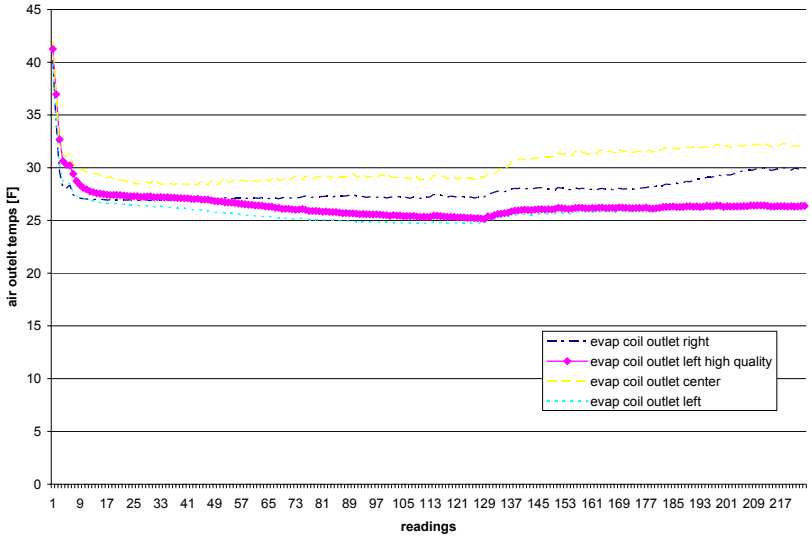

Figure A.4 Prototype-1 air outlet temperature

It can be seen that there is a spatial variation in air temperatures. This is similar to the variation seen at the coil inlet, but the difference in temperature from left to right is much lower at the exit. The lower difference in temperatures from left to right could be due to the mixing occurring as the air moves over the coil. Given the lack of a numerical value for the air-flow distribution, the average of the readings is used to represent the air outlet temperature (the HQ measurement at the left side being substituted for the other temperature reading at that location.)

The air outlet humidity is measured using 2 dew point meters and 2 relative humidity measurements (which includes one grid based measurement). The two relative humidity readings were converted to equivalent dew point values using the air temperature at that point. The 4 dew point values thus obtained were averaged to arrive at the air outlet humidity. In some data sets, the grid measurement was either erratic or too far from the other readings and had to be omitted while averaging

A.1.6 Refrigerant outlet state

The refrigerant outlet state is given by a pressure reading and a immersed thermocouple temperature reading. The evaporator pressure is important from the controls point of view. The controls installed aim at controlling the air temperatures by controlling the suction pressure, reducing it as the frost builds on the coil to maintain a constant DAT. This makes the refrigerant pressure an important parameter in the simulation of the coil. Also, given the nature of the controls, observing the variation of pressure over time gives clues regarding the degradation in airside temperature control. As an example, the evaporator exit pressure is shown in Figure A.5. After a certain time interval, the evaporator pressure drops and starts behaving erratically suggesting that the discharge air temperature is no longer constant

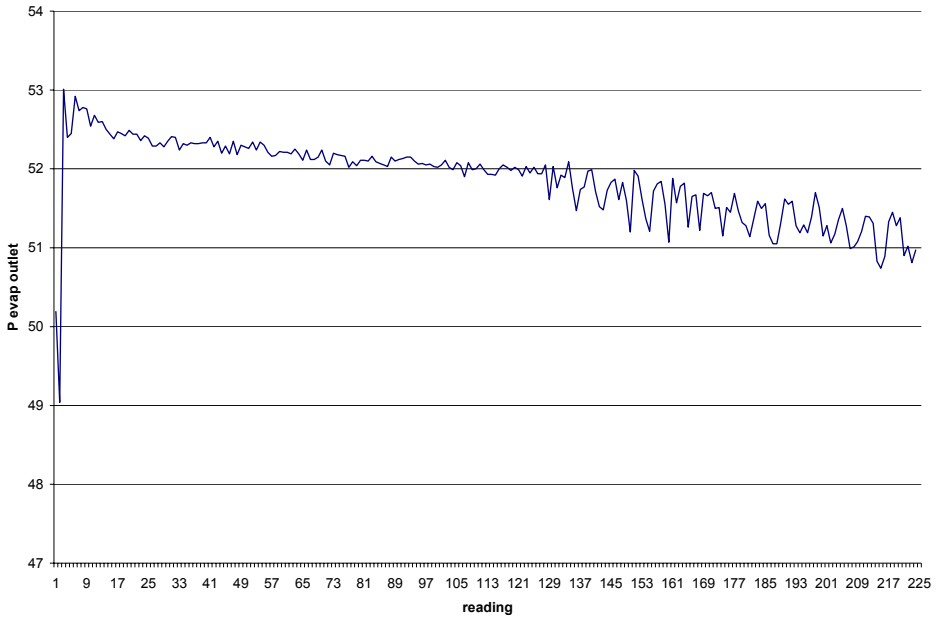

Figure A.5 Evaporator outlet pressure for the Hill Phoenix coil

As long as the refrigerant at the exit is superheated, the temperature and pressure readings are sufficient to describe the refrigerant outlet state. The Hill Phoenix coil and an initial test of the Prototype-1 coil used a TXV while later tests used an EEV for controlling the superheat. The superheat in the Hill Phoenix coil was on an average 5.8 C whereas in the August and September tests of the Prototype-1 coil, the superheat turned out to be as low as 1.2 C. These very low superheats are suspect at this stage and there is a possibility that the refrigerant does have some 2-phase component which could affect the validity of energy balance equations. This issue is dealt with in a subsequent section. A 2-phase component could in theory also affect the pressure drop readings (due to the fact that the meters are designed for either wet or dry operation)

A.1.7 Refrigerant mass flow rate

The refrigerant mass flow rate is available from the measurements made using a Coriolis mass flow meter. The measurements are as shown in Fig. A.6

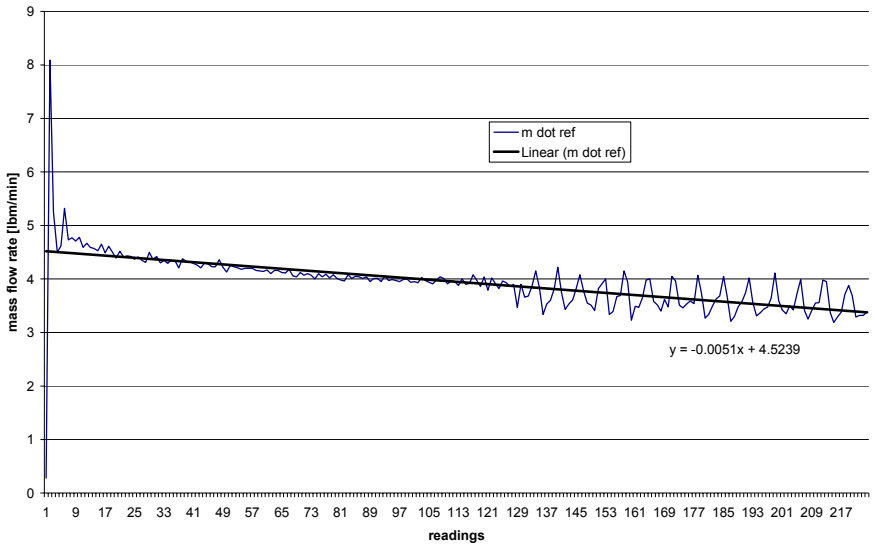

Figure A.6 Hill Phoenix baseline coil refrigerant mass flow rate

The refrigerant mass flow rate readings show large local variations and given that the simulation is sensitive to the changes in the mass flow rates, it is necessary at times to fit the values to a linear trend. The reason for large fluctuations in the refrigerant mass flow rate is not entirely known. All that is known is that the TXV (or EEV) is designed to maintain a constant superheat by controlling the mass flow rate. The most probable reason for the variations seen is the TXV (or EEV) based control. Other possible reasons include flashing in the mass flow meter or elsewhere in the refrigerant.

A.2 Comparison of experimental data and modeling results

The following graphs compare the model predictions and experimentally measured values for the Hill Phoenix coil. The validation for the other coil is very similar to that presented here for the HILL PHOENIX coil.

A.2.1. Refrigerant mass flow rate

Figure 2.2.1.1 shows that the predicted and the actual mass flow rates agree to a significant extent for most of the refrigerant period. The model does not predict the decrease in the mass flow rate seen towards the later part of the refrigeration cycle

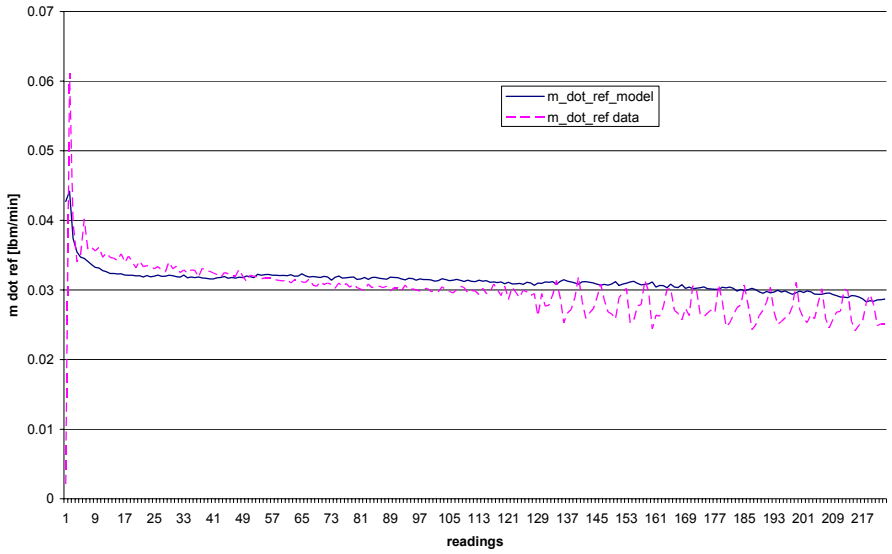

Figure A.7 Refrigerant mass flow rate comparison

A.2.2 Heat transfer rate

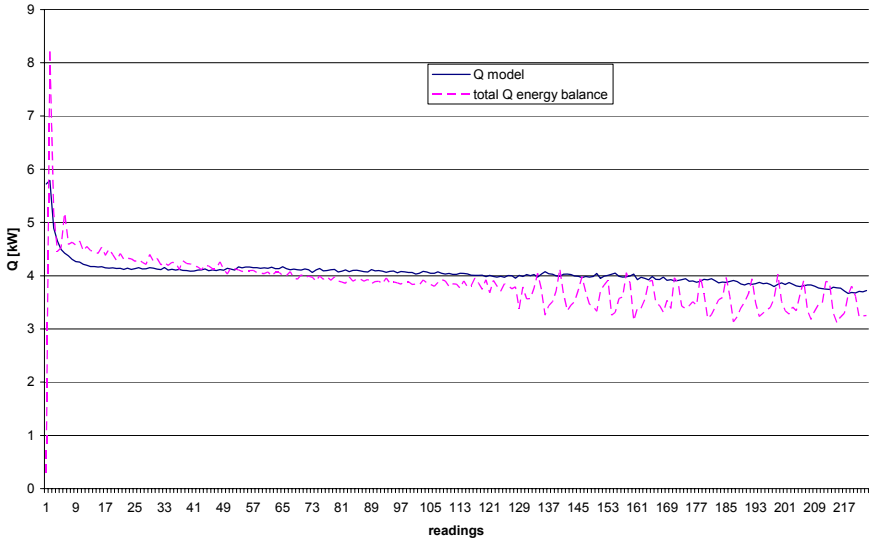

Figure A.8 Comparison of heat transfer rate

The heat transfer predictions, similar to the refrigerant mass flow rate predictions, agree well with the heat transfer values obtained from the experimental data. Once again the fall in the heat transfer rate is not predicted towards the end of the refrigerant period.

A.2.3. Mass of frost

The measured data will not be able to give us the instantaneous amount of frost present on the coil. We can infer the amount of frost accumulated on the coil during a particular refrigeration period using measured data for the amount of water collected during the defrost period that follows the refrigeration period. The model, on the other

hand, calculates the instantaneous frosting and the spatial distribution of frost. Thus the validation of the frosting aspects of the model is limited to a crude comparison of the total amount of frost accumulated over the entire refrigeration period.

The model predicts ~13.5 kg of frost accumulation over the entire refrigeration period whereas the measured amount of water collected is ~ 12.95 kg.

A.2.4. Air outlet temperature

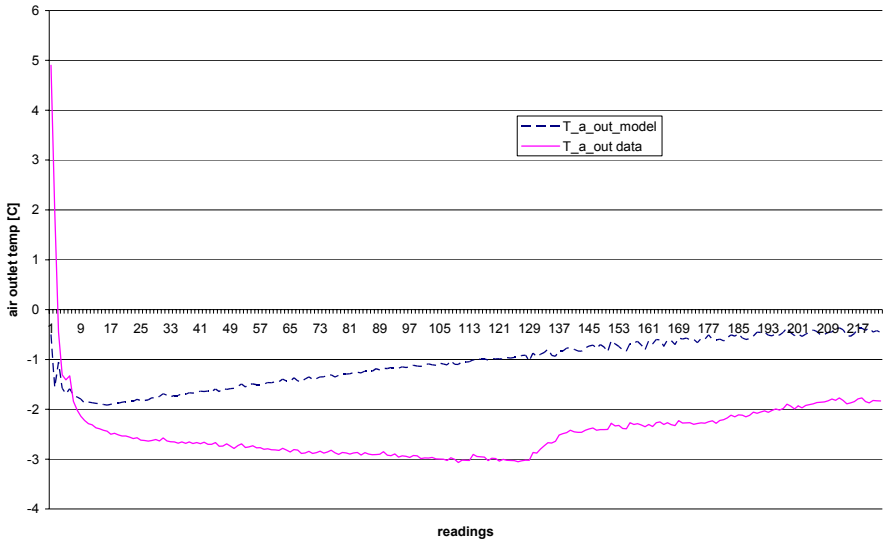

Figure A.9 Comparison of air temperature at the outlet of the evaporator coil

As seen the predicted and the measured data vary significantly. The difference is almost two to three degree C. The agreement is much better in the tests on the Prototype-1 coil, suggesting that airflow nonuniformity may be a contributing factor. However it is still significant (around 1 to 1.5 C difference)

A.2.5. Refrigerant outlet temperature

The graph shown below compares the refrigerant temperature predicted by the model and that measured at the outlet of the coil. The agreement is very good which is not surprising given that the superheat, evaporator exit pressure and inlet enthalpy are inputs to the model. What is significant however is the agreement between experiment and model over time, as the pressure drop correlations and fan curve and entrainment rates determine changes in inlet air flow rates and humidity.

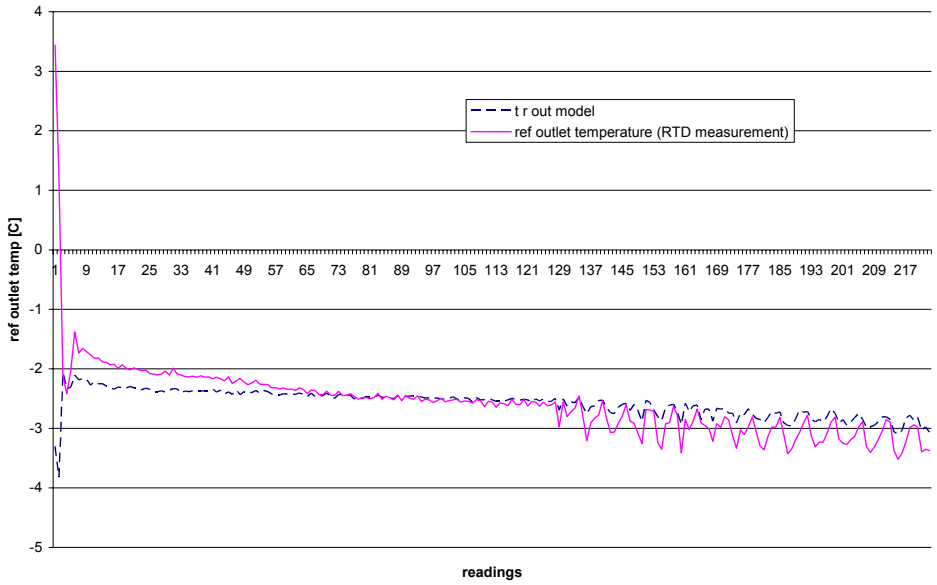

Figure A.10 Comparison of outlet refrigerant temperature

A.2.6. Air flow rate through the evaporator coil

Figure.A.11 compares the airflow rates obtained by the energy balance and the airflow rate predicted by the model. The model prediction is on the basis of the initial cfm obtained from the energy balance and the fan curve provided by the manufacturer. It is obvious from the graph that the energy balance reveals a far steeper fall in the airflow rate as the frost builds up compared to the prediction of the fan curve based model.

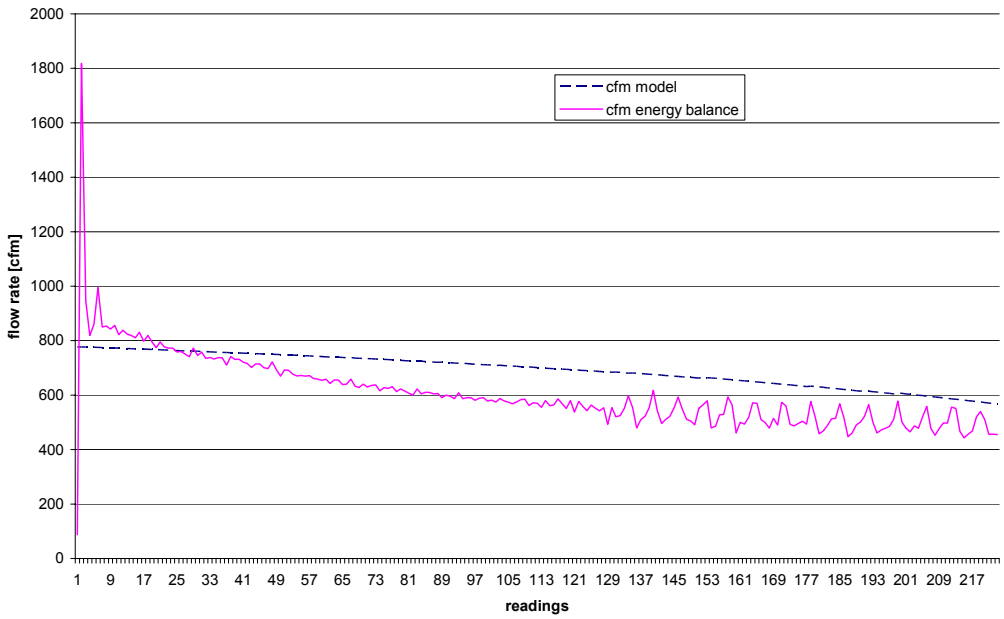

Figure A.11 Air flow rate (cfm) comparison

Appendix B. Additional Information from Experimental Data

B.1 Energy balance results

The energy balance is simply the equating of the airside and refrigerant side energy equations. The only unknown is the mass flow rate of air (the refrigerant side being completely known and the air inlet and exit states being known). The energy balance is as good or bad as the values used for the various air-side and refrigerant-side properties. The result of the energy balance for the Hill Phoenix coil is shown in Figure B.1

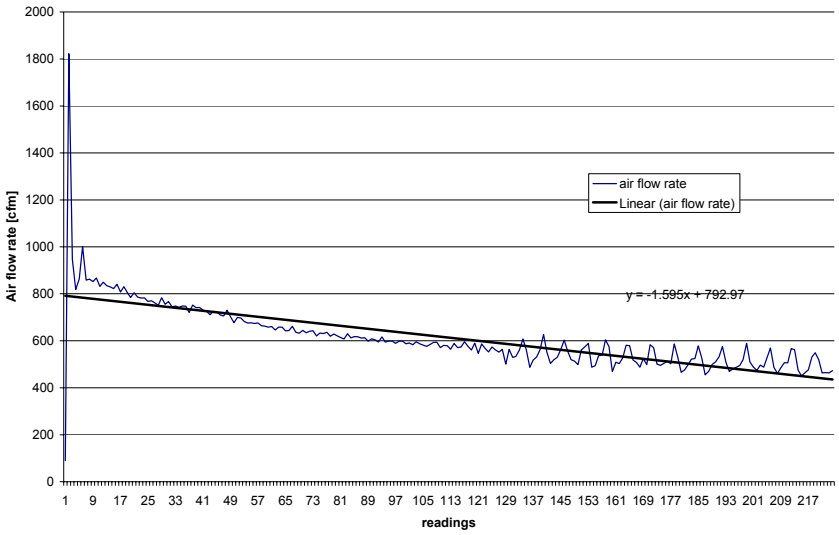

Figure B.1 Air flow rate calculated by equating energy balances

The overall trend appears to be linear. Hence doing a linear fit, we get a value of around 795 cfm as the initial airflow rate which is pretty close to the value predicted using the CFD methods (780 cfm, Faramarzi et al. 2003).

Use of the same technique for the other data sets resulted in dry coil airflow estimates. But when the EEV was used, the mismatch between the values obtained by CFD techniques (Faramarzi, 2003) and the predictions of the energy balance was significantly higher. The very low superheats maintained are theorized to be the reason. There is a significant possibility that the refrigerant is not superheated but contains droplets. Neglecting the existence of these droplets overestimate the refrigerant-side heat transfer and will result in an overestimation of the airflow rate. An example of such a case is the September 2003 tests on the Prototype-1 coil. The airflow rate estimated by energy balance is shown in Figure B.2. As seen in the figure, the initial flow rate is around 950 cfm. The value provided for the initial flow rate by SCE's CFD calculation is 750 cfm. Thus the energy balance fails to correctly estimate the air flow rate. In such cases, the CFD-based values had to be relied on as they were the only ones available.

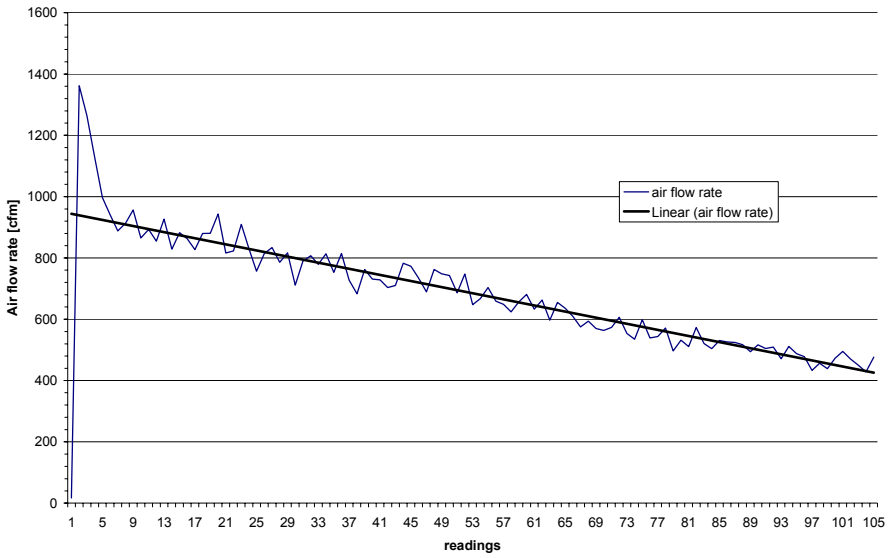

Figure B.2 Air flow rate calculated by energy balances for Prototype-1

Thus, of all the inputs to the simulation, the most suspect is the airflow rate. Part of the reason is the uncertainty involved in the estimation of the initial flow rate. The other bigger uncertainties involved are the fan performance curves and the value of the duct pressure loss.

B.2 Duct pressure loss

The dry coil air pressure loss in the evaporator is calculated using published correlations corresponding to the geometry of the evaporator. The duct pressure loss on the other hand is much more difficult to calculate given that the duct is not uniform throughout the airflow path. The duct is hence assumed to be a rectangular duct with air flowing through it. Hence the duct pressure loss is given by

$$dP_{duct} = 0.5 \cdot C_d \cdot \rho_{air} \cdot V_{air}^2 \tag{B.1}$$

Thus the duct pressure loss can be calculated when the airflow rate and the coefficient of pressure loss are known. The coefficient of pressure loss is estimated using Equations B.1-B.4 which includes the manufacturer's fan curve and the appropriate correlation for coil pressure drop (depends on the geometry).

$$dP_{duct} + dP_{evap} = dP_{fan} \tag{B.2}$$

$$dP_{evap} \Rightarrow f(cfm, geometry) \tag{B.3}$$

$$dP_{fan} \Rightarrow f(cfm) \tag{B.4}$$

Thus the coefficient of pressure loss in the duct can be found when the airflow rate is known. Assuming the coefficient of pressure loss to be independent of the flow rate, the value estimated can be used as long as the duct is unchanged. Alternatively, if Dp_{fan} and Dp_{evap} readings are available, the coefficient of pressure loss can be

directly estimated using Equations B.1 and B.2 and then can be used in the model. Thus the data set allows two independent approaches.

The data available included fan and evaporator coil ΔP measurements. Using the airflow rate estimated by the energy balance and the fan and evaporator ΔP measurements, the coefficient was estimated to have a value of 247 (Mar 26 2003 data set, axial fan with shaded pole motor). When the axial fan was replaced by a tangential blower, the coefficient was estimated to be around 240 (June 26 2003 data set). These close values suggest consistency. But the following two figures show inconsistencies among the fan curves, the airflow rates and the measured pressure differences.

Figure B.3 and B.4 shows the fan pressure differences that would be expected at the airflow rates calculated from the energy balance. The measured values are also marked in Figure B.3.

In Figure B.3, the measured pressure drop values across the evaporator increases from 0.01" (dry) to around 0.1" (frosted) which is a increase of 0.09". The pressure difference across the fan should change by an identical amount, assuming duct geometry remains constant. The measured values, however, increase from 0.08" to 0.14" or only 0.06" compared to the 0.09" seen across the coil. As seen from Figure B.3, such a large increase in the pressure drop will result in a much larger change in the air flow rate than predicted by the energy balance. So these two measurements are clearly inconsistent. It appears that the ΔP_{evap} measurement is incorrect, because the fan curve indicates that the effect of frost would decrease flow rate by more than 400 cfm. The dry coil ΔP_{evap} as predicted by correlations for this coil is 0.03" of water which is much higher than the measured value.

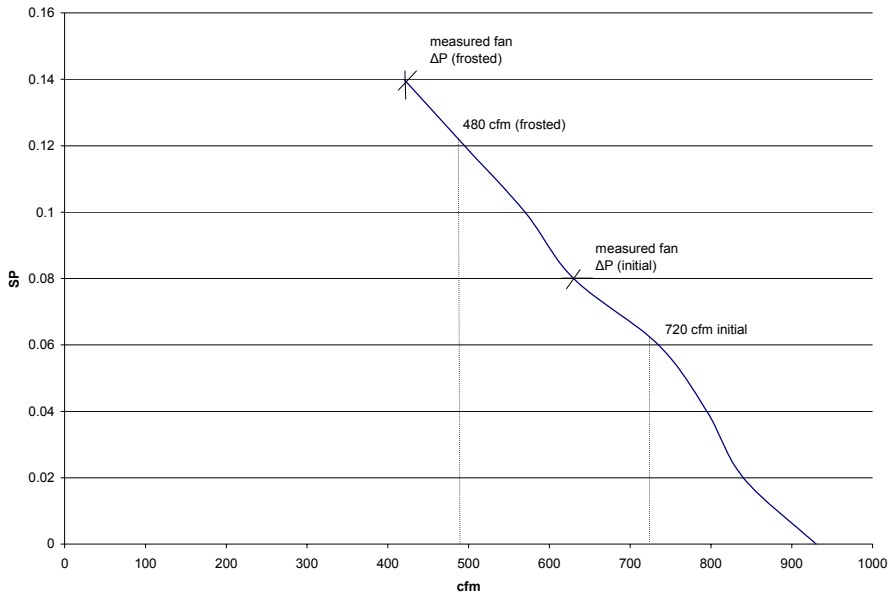

Figure B.3 Axial fan with SP motor

In Fig B.4, the measured pressure difference across the fan was 0.1" of water in the dry condition and 0.14" of water in the frosted condition. Both of these lie outside the range of the fan curve shown in Figure B.4 implying that the flow rate in the dry condition should have been less than 400 cfm and fallen even further as the coil frosted. The energy balance on the other hand suggests a fan pressure difference in the range of 0.075" of water to 0.09" of

water. These values suggest a pressure drop increase of less than 0.02" of water due to frosting. During the same experiment the measured evaporator pressure drop increased from 0.01" of water to 0.07" of water. According to Fig B.2, such an increase in pressure drop will result in a very large decrease in the airflow rate (much larger than that indicated by the energy balance).

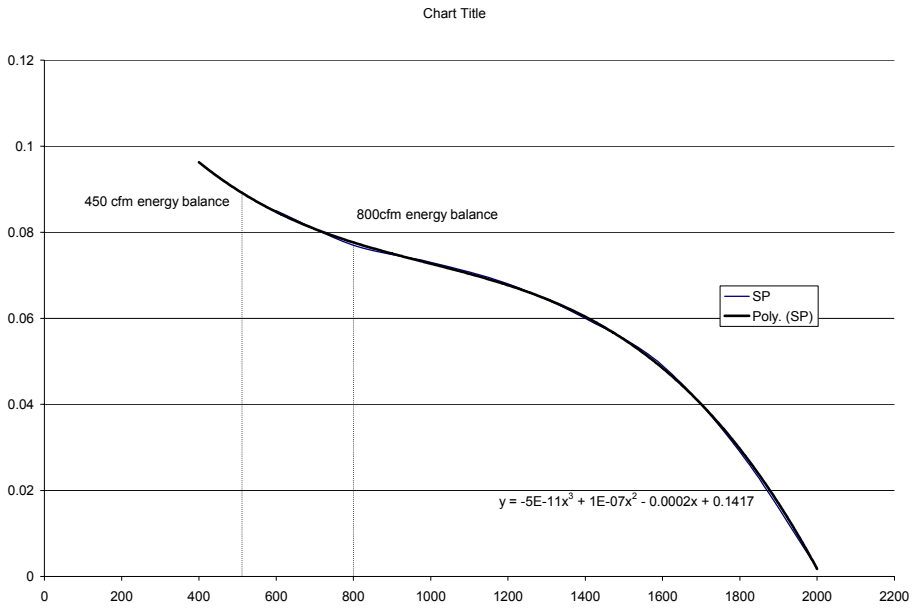

Figure B.4 Tangential fan performance curve.

Thus, the combination of the fan curve and the energy balance yield results quite different from the measured values. Given that the measured values appear to be inconsistent even among themselves (increase in fan pressure drop turning out lower than the increase in evaporator pressure drop), the measured values cannot be used to find an estimate of the coefficient of pressure loss. Hence, all 4 equations above will be needed to find the coefficient of pressure loss. The coefficient of pressure loss estimated by this method turns out to in the range of 80-90 (using the original Hill-Phoenix coil data, this turns out to be 95).

B.3 Load due to radiation and other unknown sources

Display case loads arise from infiltration of store air (~80%), radiation (~10%), accessories, transient pull-down loads, and other not easily quantifiable sources like conduction through the wall. Given the importance of knowledge of the total load during the designing of a new coil, it is necessary to estimate all the components. The loads from anti-sweat heaters, fans, lighting can be easily measured. Estimation of the radiation load and other loads has to be done using an indirect method based on the energy balance. The transient startup loads on the system do not affect the steady state operation of the coil and are tougher to evaluate. Their evaluation is not covered here.

The analysis presented gives us the values of the infiltration and the total load on the system. Figure B.5 and Equation B.5 describe the energy balance for a control volume containing the air inside the air curtain and display case. The sum of the sensible loads other than the entrainment is shown as $Q_{combined}$. It is assumed that the temperatures and humidities do not change much from the evaporator outlet to the discharge air grille and from the

return air grille to the evaporator inlet. The infiltration fraction *f* indicates the amount of ambient air entrained in the air curtain. Using these assumptions, the load balance is given as

$$Q_{evap} + f \cdot \dot{m}_{air} \cdot h_{return} = Q_{combined} + f \cdot \dot{m}_{air} \cdot h_{ambient} + Q_{fan} \quad \text{(B.5)}$$

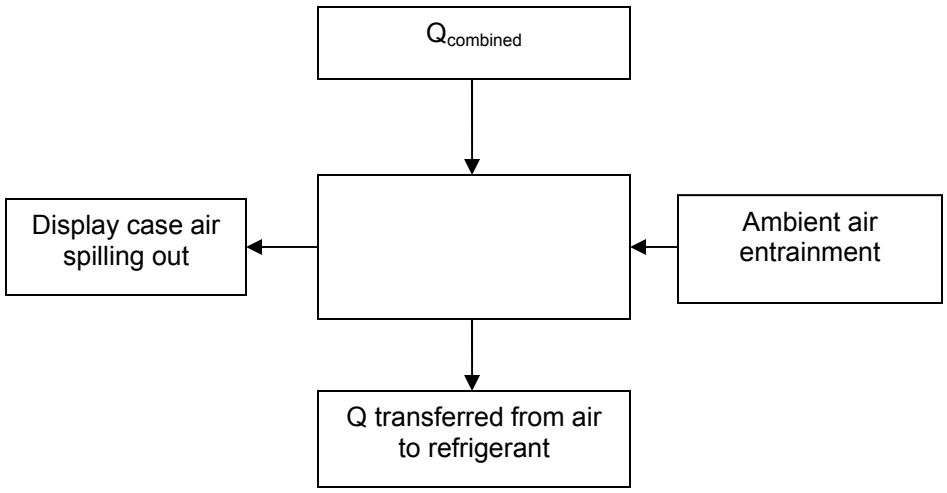

Figure B.5 Display case energy balance

Similarly, considering the control volume constructed by considering the portion of the air curtain between the discharge air grille and the return air grille, the mass balance can be written as shown in Equation B.6. It assumes that the air that spills over from the air curtain has the same temperature and humidity as the air that enters the return air grille

$$w_{dis} + f \cdot w_{amb} = (1 + f) \cdot w_{ret} \quad \text{(B.6)}$$

On the basis of these two equations, experimentally-determined data and the airflow rate, it is possible to find the entrainment fraction and the sensible loads arising due to sources other than infiltration.

The results of such an analysis are shown in Figure B.6. The plot for the combined load shows three distinct regions. The first region shows a value of load higher than the average as the product load and coil are cooled after the defrost cycle. The second region shows almost constant load and the third region shows a load lower than the average (the drop is seen for the period where the evaporator pressure drops). The value of the loads other than the entrainment is expected to remain constant. Thus the second region corresponds to the constant steady state non infiltration load and includes the entire accessory load, radiation load, conduction load and other unknown loads. This value is expected to remain constant as long as ambient conditions and the accessories remain unchanged. It is also possible to subtract the value of the known non infiltration loads from this newly arrived at value and get an estimate of the sum of the radiation load and other unknown constant loads.

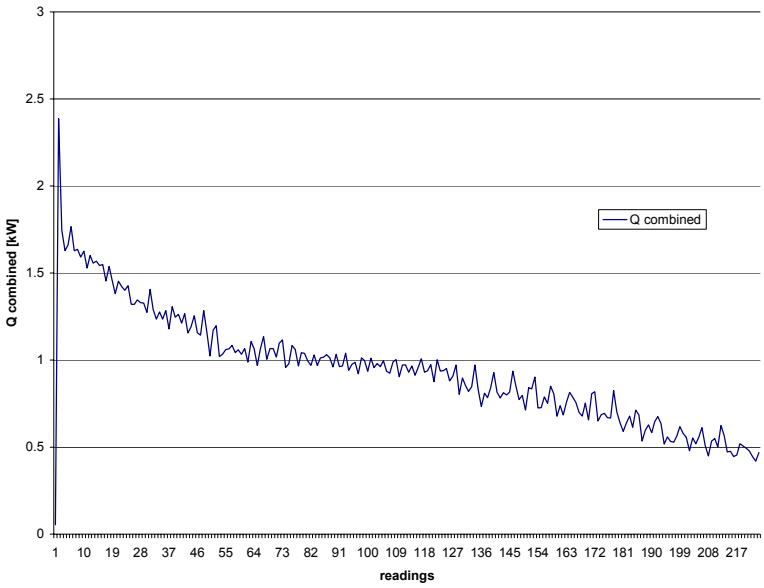

Figure B.6 Display case loads other than infiltration.

The third portion of the load curve shown in Fig B.6 cannot be explained by thermal capacitance of the product alone (using data indicating a slight temperature increase late in the cycle). The drop seen in the third module of Fig B.6 appears in the same time interval where most of the experimental data values show noisy behavior and where the suction pressure drops. Thus the drop in load seen in Fig B.6 towards the end of the refrigeration period could be the result of the controls employed in the system or the failure of the same as frost accumulates.

Appendix C. Fin Staging and Free Flow Area

A non-obvious effect of such fin staging when the evaporator is in 2 or more modules is discussed in this appendix.

In heat exchangers the free flow area and the corresponding pressure drop are decided by the frost accumulation. When the heat exchanger is built as more than one module with different fin spacings, the available free flow area and the increase in pressure drop are decided by the fin spacings used and the relative arrangement of the two (or more) modules. It is possible that certain portions of the first module on the windward side block the airflow path to the second module. Another possibility is that the frost growing on the edges of the frosted fin bridges the spacing between the two modules. These scenarios are depicted in Figures C.2 and C.4.

As an example, a coil with two modules, one of 2fpi and the other with 4fpi is analyzed. Two different arrangements for such a coil are shown in Figure 3.2.1.1. The schematic in Figure 3.2.1.1a shows an arrangement where the two modules are not staggered with respect to each other.

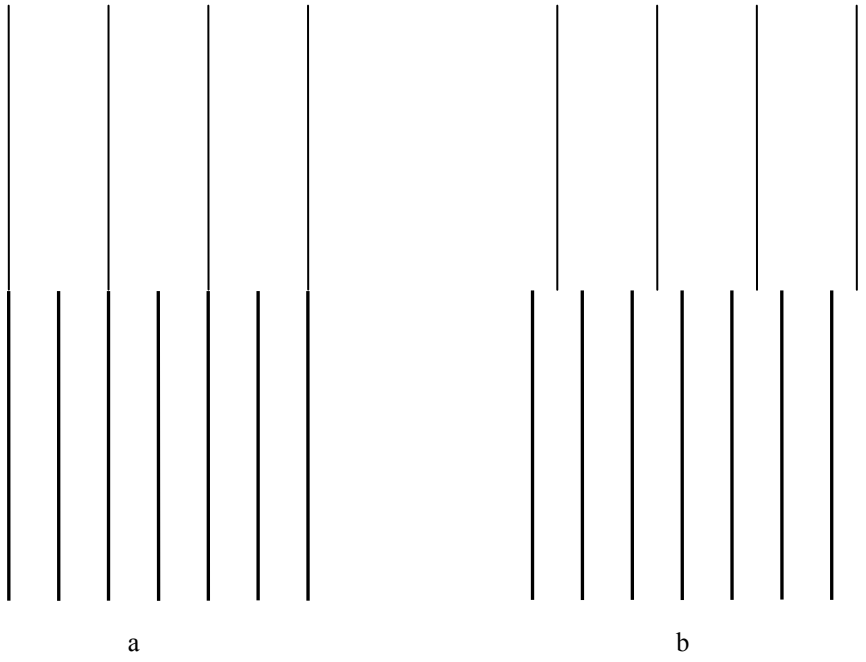

Figure C.1 Staggered and unstaggered fin staging arrangements

Figure 3.2.1.1b shows an arrangement where the two modules are staggered with respect to each other. The frosting of the two arrangements is shown in Figure C.2. In the coil where the two modules are not staggered the minimum flow area is decided purely by the initial fin spacing and thickness of frost accumulated. The frost thickness on the last row of the first module (2fpi module) and the first row of the second module (4fpi module) of the coil is very similar (actually, the frost thickness on the first module is slightly greater. But for the sake of maintaining uniformity between the various fin staging schemes, the two thicknesses are assumed to be the same). Hence the minimum flow area will be decided by the fin spacing in the second module and the frost accumulated on

the fins in this module. When the fins are staggered, as in the schematic in Figure C.1b, the frosted fins of the first module add to the blockage of the free flow area. As a result, the minimum flow area in certain sections of the downwind module of the staggered arrangement will be lower than predicted by the fin spacings and frost thicknesses alone.

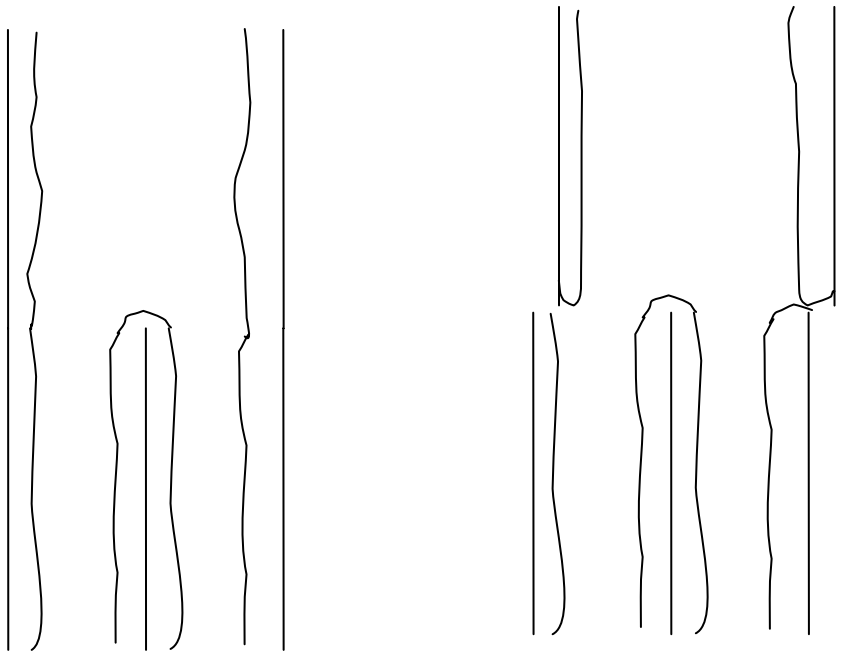

FigureC.2 Frosting of coils with fin staging

A secondary effect of this increase in flow velocities is a much increased frost deposition rate in the portions where the velocities are higher. This leads to the possibility that the narrow passage will bridge together and completely block a few of the openings to the second module. The above two figures illustrate the problems introduced when the heat exchanger is built in two modules of different fin spacings. The actual free flow area will depend on the relative fin spacings and the offset between the two modules of the heat exchangers. In the Prototype-1 coil, the first module had 2 fpi and the second module had 4 fpi and the two modules were staggered with respect to each other. When frosted, the frost of the first module can block a significant percent of the flow area of the second module. Hence at least in the portion immediately after the first module, the velocities are much higher leading to accelerated frost deposition. Hence the minimum flow area is much lower than would be expected given just the frost thicknesses and the fin spacings. Also the pressure drop across the heat exchanger increases much faster than predicted by models that don't account for the additional pressure drop due to local increases in velocity.

A photograph of the Prototype-1 coil after 3.5 hours of refrigeration is repeated in Figure C.3. The photo illustrates the effects described in the above paragraph. Some portions of the coil are almost completely blocked. The fin spacings are closer in some places than the other. This is a manufacturing issue and the resulting non-uniformity aggravates the effect discussed above.

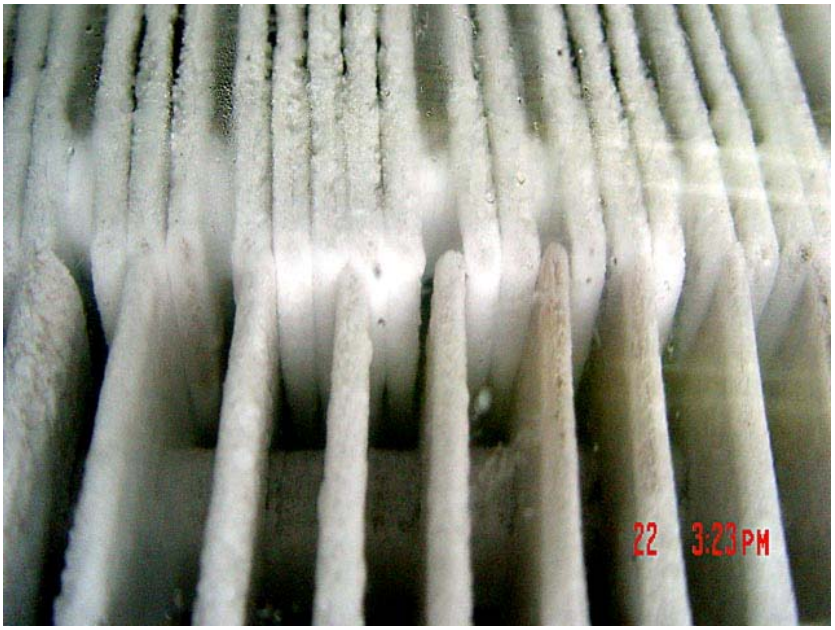

Figure C.3 Photograph of frosting of the PROTOTYPE-1 coil

On the basis of the logic discussed till here, a basic analysis was done to get a numerical estimate of the reduction in flow areas. A code was written in EES that can handle any combination of fin spacings and any value of offset (stagger) between the two modules of the coil. Results obtained are shown in Tables C.1 and C.2.

It is sufficient to analyze a 1" length in a direction transverse to the airflow in order to estimate the effect of the blockage of the first module. Referring to Figure C.1, if the second module has 4fpi, a 1" length in a direction transverse to the airflow will have 4 inter fin channels. The values in Table C.1 give the actual flow area and the increase in velocity for each of these 4 airflow paths. The actual flow area is given as a percent of the flow area that would have been available if the arrangement were unstaggered or if the additional blockage due to the first module were not present (i.e. the flow area were determined totally by the fin spacing and the frost thickness of the fins of the second module).

Table C.1 Effect of fin staggering on PROTOTYPE-1 coil (results at 3.5 hours)

Offset in mm	**Actual flow area as a percent of apparent flow area**				**V_{max} percent increase**			
	Channel 1	Channel 2	Channel 3	Channel 4	Channel 1	Channel 2	Channel 3	Channel 4
0	100	100	100	100	0	0	0	0
0.56	88	100	88	100	13	0	13	0
1.1	76	100	76	100	31	0	31	0
1.7	64	100	64	100	55	0	55	0
2.2	63	100	63	100	56	0	56	0
2.8	63	100	63	100	56	0	56	0
3.3	63	100	63	100	56	0	56	0
3.9	63	100	63	100	56	0	56	0
4.4	63	100	63	100	56	0	56	0

Table 3.3.1 illustrates the effect of staggering on the 2fpi+4fpi coil arrangement. The offset is varied from 0 mm (corresponding to no stagger) to 5 mm (the space between the fins in the 4fpi module is 6.1 mm). It is seen that in the non staggered arrangement, there is no increase in the local velocity (i.e. no local blockage). But when the offset is around 2 mm, the local velocity in half of the downwind channels is around 1.6 times larger than the velocity when the fins are perfectly aligned.

Similar analyses can be done for other fin staging arrangements. A sample analysis is shown in Table 2 for a 3fpi+4fpi arrangement. It is interesting to see that irrespective of the staggering there is the same maximum blockage in the 4fpi module due to the 3fpi module.

Table C.2 Staggering in 3fpi+4fpi coil

Offset in mm	**Actual flow area as a percent of apparent flow area**				**V_{max} percent increase**			
	Channel 1	Channel 2	Channel 3	Channel 4	Channel 1	Channel 2	Channel 3	Channel 4
0	100	63	63	100	0	56	56	0
0.56	88	63	66	100	13	56	50	0
1.1	76	63	78	100	31	56	27	0
1.7	64	63	90	100	55	56	10	0
2.2	63	63	100	97	56	56	0	2
2.8	63	68	100	85	56	45	0	16
3.3	63	80	100	73	56	23	0	35
3.9	63	92	100	63	56	8	0	56
4.4	63	100	95	63	56	0	4	56
5.0	71	100	83	63	40	0	19	56

The conclusion of the above analyses is that it is very much necessary to get a first order estimate of the increase in local velocities before employing any staging scheme. As seen from the above tables staggering may not help. In some cases it might actually worsen the pressure losses by causing local blockages and local high velocities.

In the analyses above, the two modules did not have any space between them in the airflow direction. The upwind and the downwind modules can be separated by a small distance. The effect of such spacing in the airflow direction is discussed below. As frost grows on the leading edge of the downwind fins and trailing edge of the upwind module the spacing between the two modules reduces. If the spacing between the two modules is very narrow there is a possibility that the fins of the two modules grow into each other. Such bridging of the two modules causes irregular frosting and pressure drops. Hence the spacing should at least be wide enough to prevent the frost from the two modules bridging together, and to avoid excessive increase in local heat and mass transfer which would exacerbate the bridging. Also, if the spacing is kept wide enough, it might be possible to recover some airflow area lost due to the blockage caused by the presence of the frosted fins of the first module. Moreover the presence of a space between the two modules leads to some recovery of the pressure, i.e. the pressure becomes more uniform due to a plenum effect. This leads to more uniform frosting in the second module and helps capture the full benefits of boundary layer restarting at the leading edge of the downwind module.

Figure C.4 shows a schematic of a situation where the blocking fin is midway between two fins of the second module (this is a simplifying assumption). The aim here is to calculate the separation between the two modules given the frost and fin thicknesses along with the geometry. The separation is determined such that the increase in flow area will be sufficient to overcome the loss of flow area due to blockage B. The assumption made here is that the frost grows equally on the side and the end faces of the fins at the trailing edge of the heat exchanger coil. The calculations based on basic trigonometry are detailed below. A few results are shown in Table C.3

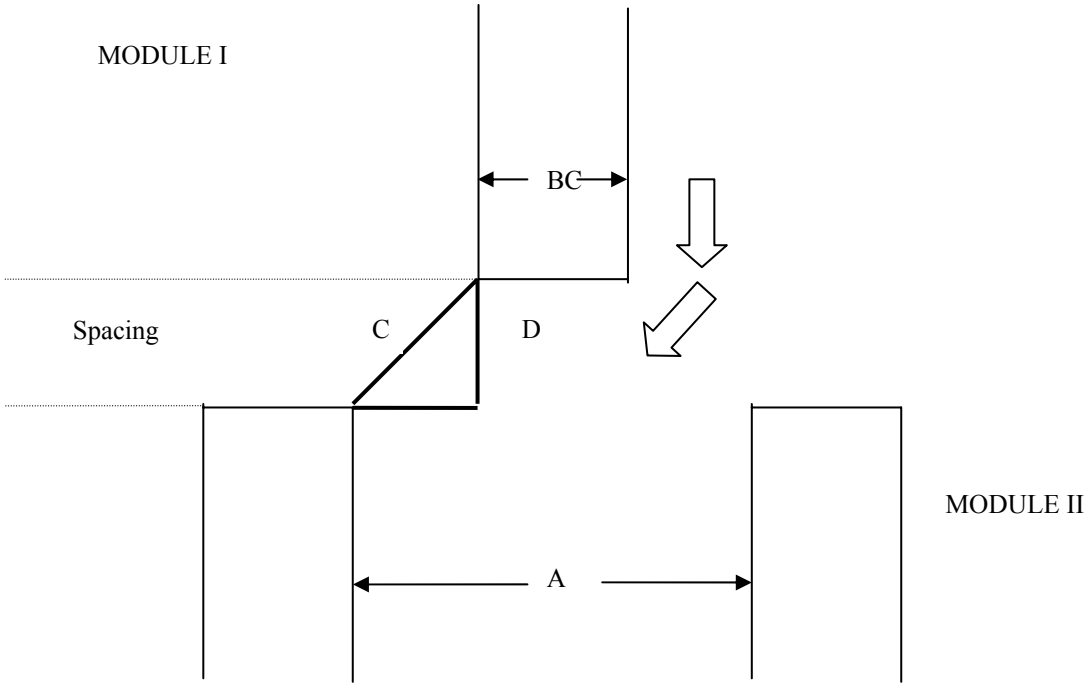

Figure C.4 Schematic depicting the spacing between the two modules of a heat exchanger

The module I fin causes a blockage equal to B. This blockage B is the sum of the fin thickness and the thickness of frost on the fin. Thus the flow area reduces from A to A-B when D=0. (The distance A is determined by the fin spacing of Module II and the frost thickness in Module II). The idea behind the spacing D is that the minimum free flow area now becomes 2C instead of A-B. By this consideration alone it is possible to determine D by noting that C is the hypotenuse of a right triangle with sides as ((A-B)/2) and the unknown D. There are other practical considerations while deciding D. The spacing should not be at the cost of heat exchanger heat transfer area. Also, the spacing will affect the size of the tube bends that will connect the two modules.

The spacing D required to compensate for the blockage B depends on the frost thickness on the fins of the two modules. We assume the same frost thickness at the trailing edge of the first module and at the leading edge of the second module. The below table shows the spacing needed as a function of frost thickness

Table C.3 Spacing required between the two modules

Frost thickness in mm	Dry coil inter module spacing required in mm
0.7	3.62
0.79	3.86
0.88	4.09
0.97	4.31
1.06	4.52
1.14	4.72
1.23	4.91
1.32	5.08
1.41	5.26
1.5	5.42

The spacing required also accounts for the growth of frost on the end faces. As seen from Table C.3, the spacing required is at the maximum 5.5mm (0.21"). This is not a large distance. Given that the above analysis was a very basic one and does not account for complications like non uniform frost growth at the trailing edge, the spacing between the modules can be made slightly larger. A spacing of around 12 mm (0.5") between the two modules should meet the purpose without causing problems from the packaging point of view.

Appendix D. A New Suction Line Heat Exchanger

Suction line heat exchangers are used to improve the performance in many HVAC&R applications using R22 or R404a as the refrigerant. Currently some display cases employ suction line heat exchangers, very simple tube-in-tube designs which are not very effective. Hence, it was decided to test the performance of a display case with a SLHX installed. This section outlines the basic heat transfer aspects of the SLHX, which was designed following the methods outlined by Boewe et al. (2001). It was installed by SCE in the display case using R404A as the refrigerant and a separate set of experiments was run in another system at ACRC using R22 as the refrigerant.

The SLHX used was a counterflow microchannel tube sandwich fabricated by Modine Manufacturing Company. The SLHX installation in the display case system is shown in Figure D.1 while the cross sectional view of the microchannel tube sandwich is shown in Figure D.2. The length of the heat exchanger was 0.97 m, and the hot and cold side perimeters and cross sectional areas were 0.17m, 0.42m and $38 \times 10^{-6} m^2$, $342 \times 10^{-6} m^2$ respectively.

Figure D.1 Installation of SLHX in a display case

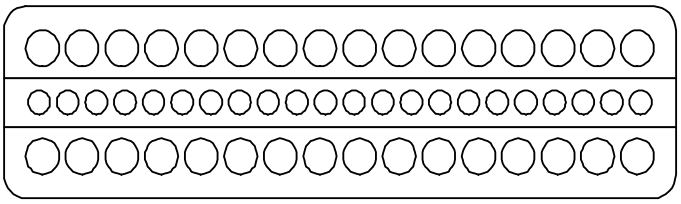

Figure D.2 Microchannel sandwich

The heat transfer performance of the SLHX is quantified by the effectiveness. The effectiveness for any suction line heat exchanger is given by

$$\varepsilon_{measured} = \frac{h_{cold,outlet} - h_{cold,inlet}}{h_{\max,cold} - h_{cold,inlet}} \qquad (D.1)$$

where $h_{\max,cold}$ represents the theoretical value of the enthalpy achieved for a heat exchanger that is 100% effective. Once the operating conditions are known it is possible to calculate the effectiveness of heat transfer.

Conventional single-phase correlations for heat transfer and pressure drop were used in the simulation program to predict the effectiveness of the counterflow heat exchanger using Equation D.2

$$\varepsilon_{theoretical} = \frac{1 - EXP(-NTU * (1 - C_r))}{1 - C_r * EXP(-NTU * (1 - C_r))} \quad \text{(D.2)}$$

where NTU is calculated using the vapor heat capacity (vapor heat capacity is lower than that of the liquid) and C_r is the ratio of vapor and liquid heat capacities. Tables D.1 and D.2 give both the theoretical (using D.2) and the measured (using D.1) effectiveness.

Table D.1 Performance of SLHX with R22 as refrigerant

m_{ref}	$T_{cold,in}$	$T_{cold,out}$	$T_{hot,in}$	$T_{hot,out}$	$\varepsilon_{theoretical}$	$\varepsilon_{measured}$
kg/s	C	C	C	C		
0.02	17.4	36.9	40.9	29.0	0.90	0.82
0.02	17.9	35.8	39.8	28.2	0.90	0.81
0.016	18.0	35.2	39.4	27.6	0.91	0.80
0.012	20.6	33.4	37.3	28.5	0.92	0.76
0.008	22.5	34.2	37.8	29.9	0.93	0.76
0.007	21.7	33.7	38	29.8	0.93	0.73
0.019	18.5	36.2	40	29.1	0.91	0.82
0.017	20.1	36.1	39.6	29.6	0.91	0.82
0.018	23.1	36.9	39.8	31.9	0.91	0.82

Table D.2 Performance of SLHX using R404A as refrigerant

m_{ref}	$T_{cold,in}$	$T_{cold,out}$	$T_{hot,in}$	$T_{hot,out}$	$\varepsilon_{theoretical}$	$\varepsilon_{measured}$
kg/s	C	C	C	C		
0.02	1.72	21.4	27	7.8	0.88	0.78
0.03	2.8	20.8	28	8.6	0.87	0.76

As seen from Tables D.1 and D.2, the measured effectiveness is lower than the calculations indicate. One of the possible reasons for the discrepancy is the loss of heat to the air flowing over the SLHX (or the air surrounding the SLHX in case it is stagnant). The SCE test was done without any insulation due to space constraints. The R22 based system had some insulation over the tubes, but even here, the headers were not insulated. Other possible reasons for the discrepancy include simplistic assumptions made in the modeling; for example, the header heat transfer is not modeled.

A simple analysis was done to estimate the heat loss from the SLHX installed in the display case. The heat loss from the tubes to the air flowing over the SLHX was calculated assuming forced convection over the tubes at h~15 W/m^2K. The temperature difference between the tubes and the air was assumed to be the average of the differences at the two ends of the SLHX.

The ideal or maximum possible heat transfer in the SLHX remains unchanged due to the losses to the ambient. The actual heat transfer would improve if the loss to the air flowing over the SLHX were eliminated. When this loss was accounted for, the effectiveness of the SLHX increased from 0.78 to 0.84 for the first case shown in Table D.2.

When the header loss to the air was added to the calculated result, the effectiveness turned out to be 0.86 which is almost the same as the predicted effectiveness. Thus, the heat loss from the SLHX tube and headers can amount to as much as 8-10% loss in effectiveness, depending on the temperature difference and the natural/forced convection environment in which it is located. In most cases it is necessary to insulate the SLHX to prevent losses to the air flowing over it.